Journal of Wind Engineering & Industrial Aerodynamics xxx (xxxx) xxx

Contents lists available at ScienceDirect

Journal of Wind Engineering & Industrial Aerodynamics

journal homepage: www.elsevier.com/locate/jweia

Potential and challenges of wind measurements using met-masts in complex topography for bridge design: Part I – Integral flow characteristics

Zakari Midjiyawa [a,b,*], Etienne Cheynet [c], Joachim Reuder [c], Hálfdán Ágústsson [d], Trond Kvamsdal [b]

[a] Norwegian Meteorological Institute, Henrik Mohns Plass 1, 0313, Oslo, Norway
[b] Department of Mathematical Sciences, Norwegian University of Science and Technology, Alfred Getz' vei 1, 7491, Trondheim, Norway
[c] Geophysical Institute and Bergen Offshore Wind Centre, University of Bergen, Allegaten 70, 5007, Bergen, Norway
[d] Kjeller Vindteknikk, Norconsult AS, Tærudgata 16, Lillestrøm, Norway

ARTICLE INFO

Keywords:
Bridges
Wind measurements
Turbulence
Complex terrain
Sonic anemometer
Meteorological mast

ABSTRACT

The paper investigates the local topographic effect on the mean and integral flow characteristics recorded by sonic anemometers mounted on tall masts near the shoreline of three different Norwegian fjords. Two years of measurements are analysed, using data from 25 three-dimensional sonic anemometers mounted at heights from 12 m to 95 m above the ground. The goal is to explore the potential and challenges of using wind measurements from the masts located on the shores of the fjords in the design of planned bridge crossings. Therefore, the study explores the deviations of the mean and turbulent flow characteristics from the traditional case of flat and homogeneous terrain. Only records with mean wind speeds of 12 m s^{-1} and above at all elevations above the ground are considered due to their relevance in buffeting response, which led to the identification of a limited number of sectors representative of strong wind conditions. Mean incidence angles with absolute values above 6° and low mean wind shear are measured in several of the selected sectors. This highlights the major influence of the local terrain and vegetation around the masts on the wind conditions at the mast locations. Nevertheless, non-dimensional variance and covariance estimates of the velocity components are found to be consistent with values previously measured from bridge decks crossing narrow fjords. The paper explores also an alternative approach to compute the friction velocity, the estimation of which is challenging in a fjord-like topography. This first part of the paper focuses on integral flow characteristics, a second follow-on part will investigate in details which eddy wave-numbers are most affected by the local terrain, based on the analysis of the spectra of the velocity fluctuations.

1. Introduction

The topography of large parts of the Norwegian west coast is characterized by fjords, i.e. long, deep inlets of the sea, typically surrounded by steep mountainsides. The largest ones are several kilometres wide and reach up to 200 km inland. A few years ago, the Norwegian Public Road Administration (NPRA) started with the major infrastructure project Ferjefri E39, aiming to realize a 1000-km ferry-free highway route along the west coast of Norway (Samferdselsdepartementet, 2013). The plans include several multi-kilometres fjord crossings by both bridges and tunnels.

The proposed bridges will be particularly sensitive to wind loading and the analysis of the flow conditions is therefore of crucial importance for their design (Scanlan, 1978; Davenport, 1961b). Among the different types of wind loading, those induced by turbulence, i.e. buffeting loads, are of major interest (Delaunay and Grillaud, 1998; Cheynet et al., 2016). The flow field over the fjord, in the vicinity of steep mountain slopes, will be strongly affected by topographic effects, such as channelling (Jackson and Steyn, 1994), downslope wind storms (Sandvik and Harstveit, 2005), and extreme gusts (Grønås and Sandvik, 1999), e.g caused by turbulent eddies, either generated locally due to flow over or along complex terrain (Ágústsson and Ólafsson, 2004), or aloft in steep and possibly overturning gravity waves (Guarino et al., 2016).

These fine-scale flow features challenge the identification of the flow characteristics used to model the wind load on slender structures such as long-span bridges. Earlier studies of relevance have been performed for

* Corresponding author. Norwegian Meteorological Institute, Henrik Mohns Plass 1, 0313, Oslo, Norway.
E-mail address: midjiyawaz@met.no (Z. Midjiyawa).

https://doi.org/10.1016/j.jweia.2021.104584
Received 26 October 2020; Received in revised form 20 January 2021; Accepted 17 February 2021
Available online xxxx

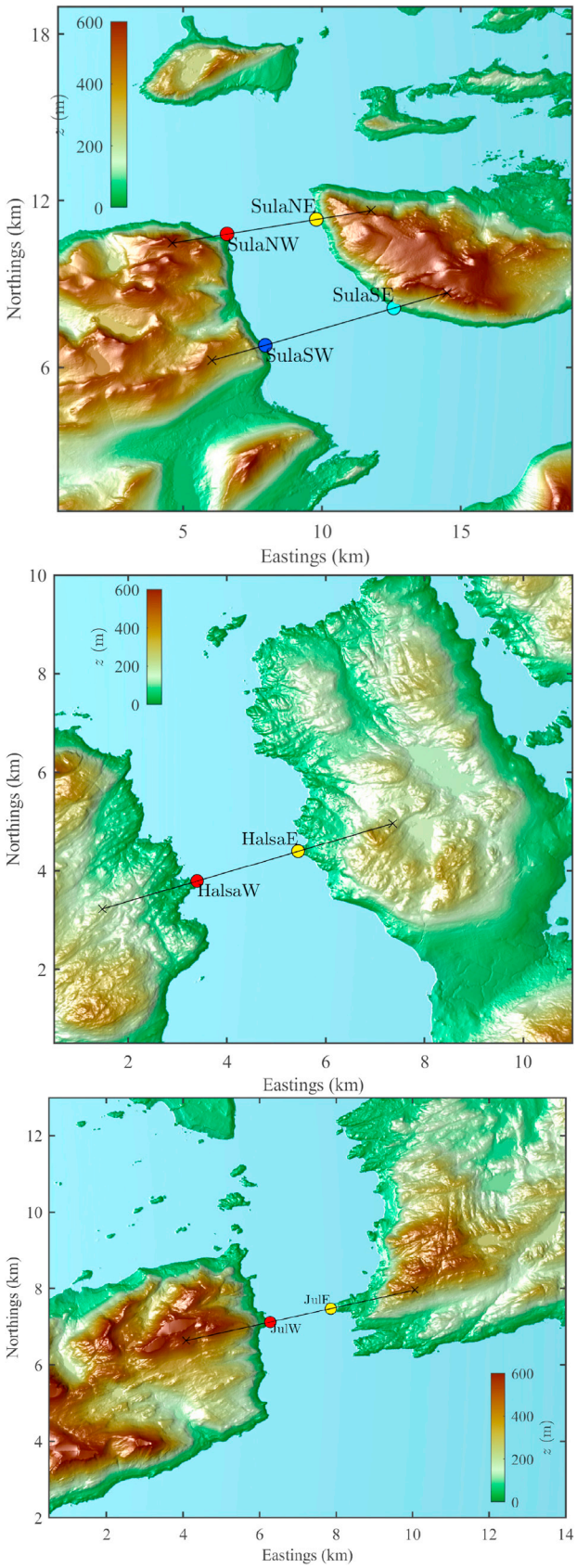

Fig. 1. Digital terrain models with a horizontal resolution of 10 m illustrating the location of the measurement masts and the surrounding topography for, from top to bottom, Sulafjorden, Halsafjorden and Julsundet.

the Saint-Nazaire bridge in western France (Sacré and Delaunay, 1992; Bietry et al., 1995) for two distinctive winds directions with different upstream roughness, the Iroise cable-stayed bridge (Delaunay and Grillaud, 1998), also in western France, and the Stonecutters Bridge in Hong Kong (Hui et al., 2009a,b), to name a few. Detailed investigated bridges at the Norwegian west coast are the ones crossing the Lysefjord (Cheynet et al., 2016, 2017b), the Hardangerfjord (Fenerci et al., 2017; Fenerci and Øiseth, 2018a,b) and the bridge connecting Bergen with the island of Sotra (Jensen and Hjort-Hansen, 1977). These studies are, however, very specific and focus on a single site. There exists only a limited number of studies discussing turbulence characterization from multiple Norwegian fjords (Harstveit, 1996; Cheynet et al., 2019). It is still an open question whether the wind conditions in fjords can be studied adequately by only using met-masts installed on the shore and if the wind flows in such locations share common turbulence characteristics. The present study uses wind measurements from eight masts in three different fjords, providing a unique opportunity to discuss this open question.

The paper aims at investigating the potential and limitations of using velocity data recorded on tall masts, located on the shore of fjords surrounded by steep mountains, for the computation of the dynamic wind load on long-span bridges. The fjords of interest in this work are Sulafjorden, Halsafjorden, and Julsundet. In each of them, two to four masts, each mast carrying three to four sonic anemometers, were installed on the seaside. The study, which is based on two years of wind measurements, is split into two parts. The first part, presented hereafter, focuses on assessing the influence of local topography on the mean flow and the integral turbulence characteristics. In particular, the mean incidence angle, the deviation from the assumption of Gaussian fluctuations, as well as the variance and covariances of the velocity components, are investigated. The so-called "integral turbulence characteristics" represent here the characteristics that can be retrieved by integrating the spectral, and cross-power spectral densities of the velocity fluctuations over the frequencies. The second part, subject to a separate publication, investigates the influence of local topography on turbulence in the frequency space.

The present paper is organized as follows: Section 2 describes the topography surrounding the different met masts as well as the experimental setup. Section 3 summarises the data processing with a focus on data reduction to isolate records relevant to bridge design. Section 4 quantifies the deviations of the flow characteristics from the assumptions of horizontal mean flow and Gaussian fluctuations. The impact of the local terrain on Reynolds stress tensor is also explored. Finally, Section 5 summarises the challenges associated with the measurement of turbulence close to mountainsides.

2. Measurement locations and observation setup

Fig. 1 shows an overview of the topography at the fjords of interest, with markers indicating the position of the respective met-masts. The observation sites are located in the Møre and Romsdal county of western Norway; a mountainous region characterized by a large variability in surface roughness and land type (Fig. 2).

Sulafjorden is more exposed to the open sea from its northwestern side, compared to Halsafjorden and Julsundet, which are located more inland with mountains on their east and west side. Sulafjorden is surrounded by mountains with heights up to 900 m. To the north and the south at SulaNW and SulaNE, the wind has a long fetch over open water. Towards the northwest and southeast at SulaNE, sectors associated with an onshore flow are typically characterized with high and variable roughness, due to a combination of steep and rough terrain as well as a varying vegetation cover.

Topography profiles across the relevant fjords, through the mast locations, are presented in Fig. 3. All the masts are located near the shoreline, but local conditions dictate that many of them are located in steep terrain or on top of small headlands. Potential local topographic effects have, therefore, to be taken into account when analysing the

Fig. 2. Overview map showing the location of the three fjords under investigation in this study.

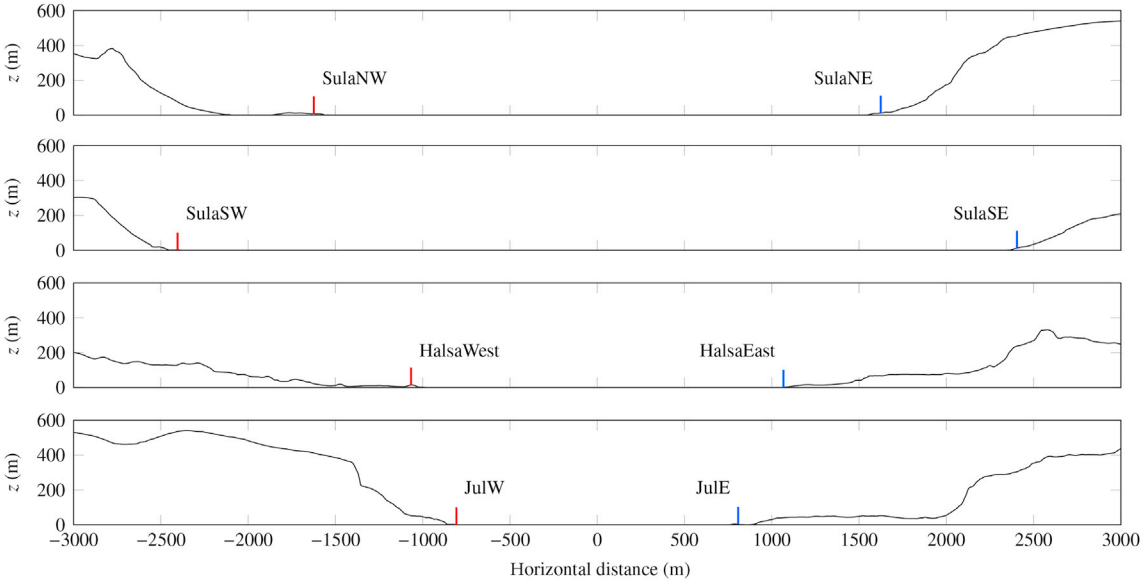

Fig. 3. Overview of the mast positioning and height compared to surrounding topography.

observations (Ishihara et al., 1999).

Since 2014, eleven met-masts have been installed on the seasides of Sulafjorden, Halsafjorden and Julsundet. Data from eight of these masts are explored in the present study. Two met-masts each were deployed on the western and eastern sides of Halsafjorden and Julsundet, in the following denoted as HalsaW/HalsaE and JulW/JulE, respectively (Fig. 1). At Sulafjorden, four met masts were installed along two E-W transects, correspondingly labelled as SulaNW, SulaNE, SulaSW, and SulaSE (Fig. 1). The distance between the two masts in each transect is approximately 3 km and 4 km, respectively.

A detailed description of the measurement setups, including instrumentation, sampling rate, local surface characteristics and topography is given in Furevik et al. (2020). A summary is presented hereafter, for the sake of completeness. Five of the eight masts are lattice structures whereas the other three, at Julsundet and on the western shore of Halsafjorden, are guyed tubular masts (Fig. 4). The coordinates, mast heights, boom orientation, measurement heights above the terrain, and observation periods are summarised in Table 1. The tubular masts are 250 mm–300 mm in diameter, while the lattice towers horizontal dimensions vary from 60 cm to 2.6 m. Boom lengths and directions were

Fig. 4. Examples of mast structures used. Rectangular lattice tower at Aakvik in Halsafjorden (upper left), Kvitneset in Sulafjorden (upper right), and Halsaneset in Halsafjorden (below), where one of the anemometers can also been seen. Photos: Kjeller Vindteknikk.

chosen to minimize possible tower disturbances for the prevailing wind directions, estimated using numerical atmospheric simulations with the WRF model in a horizontal resolution of 500 m (NCAR, 2020). The velocity records from the masts show that wind directions perpendicular to the main fjord axes are relatively infrequent, and only a small amount of observations are associated with mast shadow. Each mast is instrumented with 3D sonic anemometers of the type Gill WindMaster Pro. Data were recorded by a Campbell CR 1000 logger and saved with a sampling frequency of 10 Hz. The measurements are quality checked, described and analysed in bi-annual technical reports, with the most recent ones being Ágústsson et al. (2020) and Eriksen (2020).

3. Theoretical background and data processing

3.1. Traditional assumptions in wind turbulence

The wind velocity is generally described as a tridimensional and trivariate random process in wind engineering and micro-meteorology. If the mean flow is horizontal, the along-wind, u, and cross-wind, v, components are also located in the horizontal plane. The vertical component is denoted by w. In flat terrain, the velocity components are studied in a Cartesian coordinate system $\{x, y, z\}$, where x, y and z are the along-wind, cross-wind and vertical directions, respectively. The cross-wind direction is sometimes also referred to as the lateral direction to avoid any confusion with the vertical direction. In this context, u, v and w can be decomposed into a mean component, denoted by an overbar and a fluctuating component, denoted by a prime

$$u = \overline{u} + u' \tag{1}$$

$$v = \overline{v} + v' \tag{2}$$

$$w = \overline{w} + w' \tag{3}$$

In the traditional description of atmospheric turbulence, u', v' and w' are stationary, ergodic, Gaussian random processes with a zero mean value. In particular, v and w are equal to zero, as the mean transport is assumed to occur along the mean wind direction only. Over gentle hills, the flow is no longer horizontal and $w \neq 0$. If no flow separation occurs, the flow characteristics can be studied in the mean streamline coordinate system where w is zero, which is obtained after the rotation of the coordinate system $\{x, y, z\}$ (e.g. Wilczak et al., 2001). In more complex terrains, there is no clear consensus on which coordinate transformation is best suited to study turbulence (Oldroyd et al., 2016; Stiperski and Rotach, 2016; Klipp, 2018).

The assumption of Gaussian fluctuations implies that the description of wind turbulence can be limited to the second-order characteristics, i.e. variance and covariance of the velocity fluctuations. Variance and covariance estimate can be derived by integrating their auto and cross-power spectral density over the frequencies. This justifies the term "integral" turbulence characteristics used in the following. The variance and covariance of the velocity fluctuations, also called Reynolds stresses, can be represented by the symmetric Reynolds stress tensor.

$$\boldsymbol{R} = \begin{bmatrix} u'u' & u'v' & u'w' \\ u'v' & v'v' & v'w' \\ u'w' & v'w' & w'w' \end{bmatrix} \tag{4}$$

In flat and homogeneous terrain, it is generally assumed that the only non-zero off-diagonal term is $u'w'$, i.e., the Reynolds stress is aligned with the horizontal mean wind vector. However, the term $v'w'$ is not always negligible, e.g. above the ocean (Geernaert, 1988) or in complex

Table 1
Overview of the met-masts: Mast acronym, mast location, mast height, mast type, sensor heights, boom orientation, boom length, and coordinate position. Reproduced from Furevik et al. (2020).

Mast acro.	Mast loc.	Mast h.(m)	Mast type	Sensor h. (m)	Boom orient. (Deg)	Boom l. (m)	Coord.(UTM32)
SulaNW	Kvitneset	100.5	Lattice	92.5, 71.5, 44.5	72, 74, 74	6.1	6924741 N, 345142 E
SulaNE	Trælbodneset	78.0	Lattice	76.8, 48.3, 27.3	289, 290, 290	6.1	6925267 N, 348347 E
SulaSW	Langeneset	97.0	Lattice	94.8, 75.0, 50.0, 27.0	81, 81, 81, 81	4.4	6920740 N, 346520 E
SulaSE	Kårsteinen	63.0	Lattice	62.8, 40.0, 13.4	223, 223, 223	3.6	6922074 N, 351140 E
HalsaW	Halsaneset	50	Tubular	50.3, 31.9, 12.7	106, 106, 104	1.8	6995095 N, 456472 E
HalsaE	Åkvik	50	Lattice	48.3, 31.9, 17.0	227, 227, 227	4	6995697 N, 458519 E
JulW	Nautneset	68	Lattice	68.3, 52.3, 32.7	239, 239, 239	5.1	6957381 N, 394634 E
JulE	Julbo	50	Tubular	50.3, 31.9, 12.7	234, 234, 234	1.8	6957730 N, 396210 E

terrain (Zeman and Jensen, 1987). Similarly, on the sides of a fjord, the terms $u'v'$ and $v'w'$ may no longer be negligible compared to $u'w'$, because the vicinity of the mountain slopes can be a source of additional shear stresses.

Deviations from the assumption of Gaussian flow may be observed on the shore of a fjord. Such deviations can be assessed using the skewness γ an excess kurtosis κ, which is defined as the kurtosis minus three. If the flow is Gaussian, both γ and κ are zero.

The time-average, used in the following, can be considered as equal to the true average if the assumption of ergodicity holds and if the time-averaging interval is long enough. Therefore, longer records will reduce the random error associated with the time-averaging operator. In the wind engineering community, the time-averaging interval is typically chosen to be 10 min or, more rarely, as 1 h (Cao, 2013). In the field of boundary layer meteorology, the time-averaging interval is typically in the range of half an hour to 1 h (Stull, 1988). One reason for this difference is that, in boundary layer meteorology, there is high interest in the momentum flux between the atmosphere and the surface, expressed by the covariance between the horizontal and vertical velocity components. Those fluxes require longer time-averaging intervals for sufficient accuracy compared to the variances (Kaimal and Finnigan, 1994). Time-averaging intervals beyond 1 h are seldom used as they are typically linked to non-stationary fluctuations, for which many of the tools used in descriptive statistics are no longer valid.

3.2. Friction velocity

The friction velocity is the fundamental scaling velocity in the surface layer (Kaimal and Finnigan, 1994) and can conveniently replace the variance of the velocity components to model the dynamic wind load. However, the estimation of the friction velocity can be challenging in complex terrain. Following Weber (1999), the friction velocity can be estimated after the application of the double rotation technique as

$$u_* = \left[(u'w')^2 + (v'w')^2\right]^{1/4} \tag{5}$$

Unless explicitly stated, u_* is computed in the following as in eq. (5) because directional shear is expected to play a non-negligible role in complex terrain (Rotach et al., 2008; Mahrt, 2011). If the horizontal shear stress $u'v'$ is non-negligible, the friction velocity might be computed using the invariant of the Reynolds stress tensor (Klipp and Adelphi, 2008; Klipp, 2018). The method by Klipp (2018) is an elegant approach to compute the friction velocity without using any tilt correction algorithm. Even though it was developed using a dataset collected in flat terrain, Klipp's method may become a valuable tool to study the friction velocity in complex terrain. Klipp's method is adapted to strong wind speeds and neutral atmospheric stratification. The method is summarised hereafter for the sake of completeness. First, the eigenvalue decomposition of the Reynolds stress tensor (eq. (4)) is applied, leading to the three eigenvalues, i.e., principal components of the Reynolds stress tensor, $\lambda_1 > \lambda_2 > \lambda_3$ and their associated eigenvectors $\mathbf{\Lambda_1}$, $\mathbf{\Lambda_2}$, and $\mathbf{\Lambda_3}$ (denoted Λ_b, Λ_m, and Λ_s in Klipp (2018)). Then, the friction velocity is computed as

$$u_{*_R} = \left[(\lambda_1 - \lambda_3)\cos(\beta)\sin(\beta)\right]^{1/2} \tag{6}$$

where β is the complement of the angle between the mean wind speed vector $\boldsymbol{U}$ and the vector $\mathbf{\Lambda_3}$

$$\beta = 90 - \arccos\left(\frac{\boldsymbol{U}\cdot\mathbf{\Lambda_3}}{|\boldsymbol{U}|\,|\mathbf{\Lambda_3}|}\right) \tag{7}$$

The discrepancies between u_{*_R} and u_* are investigated in Section 4.5.3.

3.3. Data selection

In the following, a subset of the complete dataset is used, i.e. observations of 2018 and 2019. The data are freely available for every met-mast (Furevik et al., 2019, 2020). Further data-processing performed for this study is described below

- The anemometer records were grouped into time series of 30 min. This ensured that a sufficiently high number of turbulent eddies is included in the calculation of the turbulence characteristics. A 30-min time-averaging is long enough to reduce the random error associated with the calculation of the Reynolds stress tensor but, at the same time, short enough to limit the number of non-stationary wind records.
- Samples with mean wind speed values lower than 12 m s^{-1} were removed. For bridge design purposes, the turbulence intensity (*TI*) of the along-wind component, denoted I_u, is independent of the mean wind speed (EN 1991-1-4, 2005). Therefore, the same I_u is valid for a wide range of mean wind speeds. In full-scale, the *TI* is defined as $I_j = \sigma_j/u$, where $j = \{u, v, w\}$ and σ_j denotes the standard deviation of the fluctuating component j. The *TI* is inversely proportional to u, leading to overestimated *TI* values at low wind speed. Furthermore, the buffeting response analysis is generally done under neutral conditions (Repetto and Solari, 2007), which are dominant under strong wind conditions (Barthelmie, 1999; Sathe et al., 2011; Cheynet et al., 2018b). In heterogeneous terrain, where multiple internal boundary layers exist, the atmospheric stability is preferably studied locally

Table 2
Cumulated absolute number N and relative number of samples, including those with $u \geq 12$ m s^{-1}, those which passed the Gaussianity test, those with low statistical uncertainties test and those stationary up to the second order, for every met-mast from the 01-01-2018 to 31-12-2019. Note that the number of samples are summed for all available anemometers.

Mast		N	Above or equal to 12 m s^{-1}	After Gaussianity test	Low statistical uncertainty	Stationary
SulaNW	Samples	65014	3890	3888	3445	2547
	100%		5.98%	5.98%	5.30%	3.92%
SulaNE	Samples	67659	3351	3347	3089	2134
	100%		4.95%	4.95%	4.57%	3.15%
SulaSW	Samples	82102	1258	1258	1214	831
	100%		1.53%	1.53%	1.48%	1.01%
SulaSE	Samples	67862	616	616	607	338
	100%		0.91%	0.91%	0.89%	0.50%
HalsaW	Samples	36696	764	758	723	537
	100%		2.08%	2.07%	1.97%	1.46%
HalsaE	Samples	55651	738	737	724	547
	100%		1.33%	1.32%	1.30%	0.98%
JulE	Samples	59215	1336	1329	1266	722
	100%		2.26%	2.24%	2.14%	1.22%
JulE	Samples	50391	1455	1454	1377	832
	100%		2.89%	2.89%	2.73%	1.65%

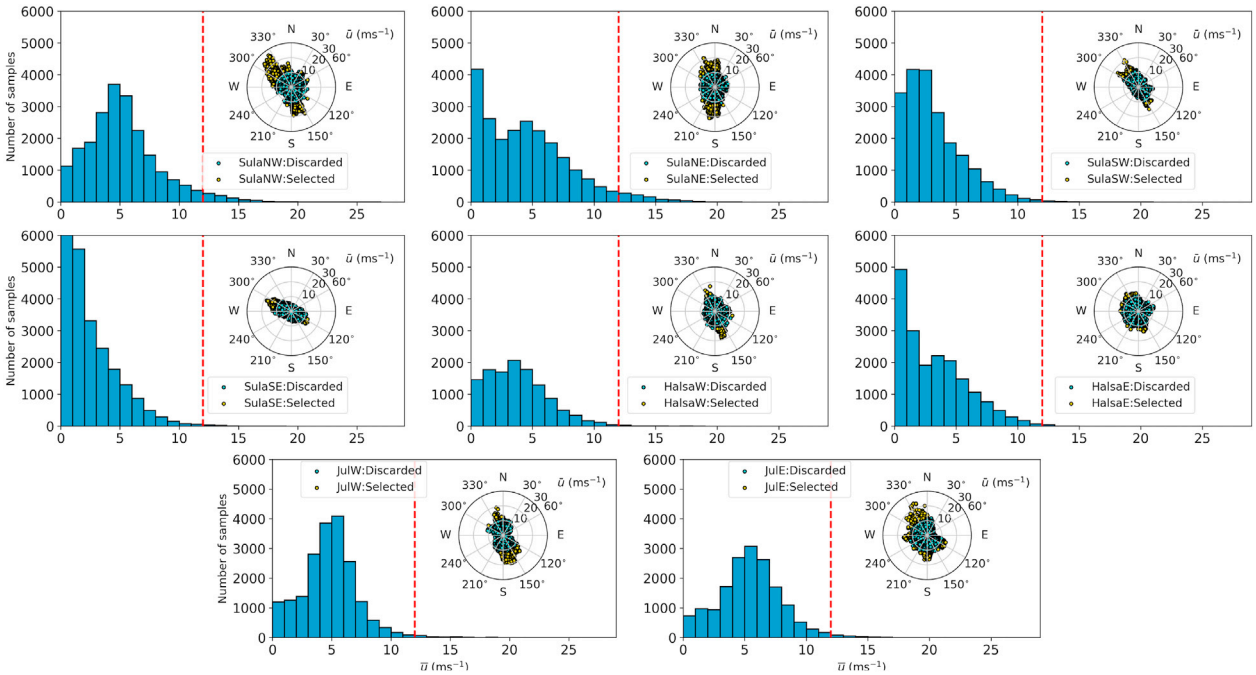

Fig. 5. Histogram and wind roses of the 30-min velocity records by the anemometer nearest to 50 m above ground level from the 01-01-2018 to 31-12-2019. The red dashed line shows the mean wind speed threshold ($u \geq$12 m s^{-1}) chosen in the data processing. (For interpretation of the references to colour in this figure legend, the reader is referred to the Web version of this article.)

using sonic anemometer data and the eddy-covariance method. The sonic temperature data were stored by the sensor on each mast and available at a sampling frequency of 2 Hz. To obtain a reliable estimate of the temperature fluxes, a sampling frequency of at least 10 Hz and ideally 25 Hz is required (Kaimal and Finnigan, 1994). Therefore, no reliable estimate of the Obukhov length could be obtained in the present case. This further motivates the dismissal of low-wind speed records.

- The double rotation technique was used to compensate for the tilt in the flow (Kristensen and Jensen, 1979; Golzio et al., 2019), as sectorial planar fit may not be appropriate in terrains with steep slopes, such as on the west coast of Norway near the masts (Klipp, 2018).
- Turbulence characteristics were analysed after the removal of linear trends. Trends come from low-frequency fluctuations not captured by the records due to their finite duration. Both linear and non-linear trends can lead to poorly estimated turbulence characteristics. To avoid over-processing of the data, only linear trends were removed in the following.
- Unphysical signals, which were characterized by an unusally high skewness and kurtosis were removed. The maximum accepted value of skewness was set to 2 and of kurtosis to 8, following the suggestions by Stiperski and Rotach (2016) and Vickers and Mahrt (1997). This step is called "Gaussianity test" in the following.
- Non-stationary samples were removed. The moving mean and standard deviation were calculated for every time series segment using a window length of 10 min. A maximum deviation of 20% is allowed for the moving mean and 40% for the moving standard deviation (Cheynet et al., 2019).
- The statistical uncertainties in the momentum fluxes were calculated following Wyngaard (1973) and Stiperski and Rotach (2016), as

$$a_{uw}^2 = \frac{z}{\tau \bar{u}} \left[\frac{\overline{(u'w')^2}}{u_*^4} - 1 \right] \tag{8}$$

$$a_{vw}^2 = \frac{z}{\tau \bar{u}} \left[\frac{\overline{(v'w')^2}}{u_*^4} - 1 \right] \tag{9}$$

where τ and z are the length of the time series and the measurement height, respectively. A limit of 50% for the statistical uncertainty was chosen (Stiperski and Rotach, 2016). Equations (8) and (9) show that long record duration results in reducing uncertainties associated with the calculation of the momentum flux. A shorter time-averaging interval has the advantage of providing more time series for the analysis. However, reducing the averaging time increases both the random error and the measurement bias, both of which increases the statistical uncertainties.

4. Results

4.1. Data availability

Table 2 shows the number and percentage ratio of available 30-min times series fulfilling the requirements for data analysis described in Section 3.3. For each met-mast, the available data are summed up for all the anemometers. This gives a general overview of the available data obtained after each filtering step.

The data processing filters out more than 90% of the velocity records. The criterion causing the largest data reduction is the minimum mean wind speed threshold, which in the present case is 12 m s^{-1}. The Norwegian fjords are typically sheltered by mountains, although, under certain conditions, flow acceleration may be locally observed. Nevertheless, it is unknown whether such speed-up events are commonly observed near the measurement sites. Although interesting, this topic is out of the scope of the present work.

The other criteria, namely the Gaussianity, statistical uncertainty, first and second-order stationarity are only filtering out a small portion of the remaining time series. After the filtering process, the highest amount of data is found to be at SulaNW and SulaNE, which highlights the higher exposure of the northern side of Sulafjorden compared to the other locations studied here.

Fig. 5 displays histograms of the wind speed, as well as the

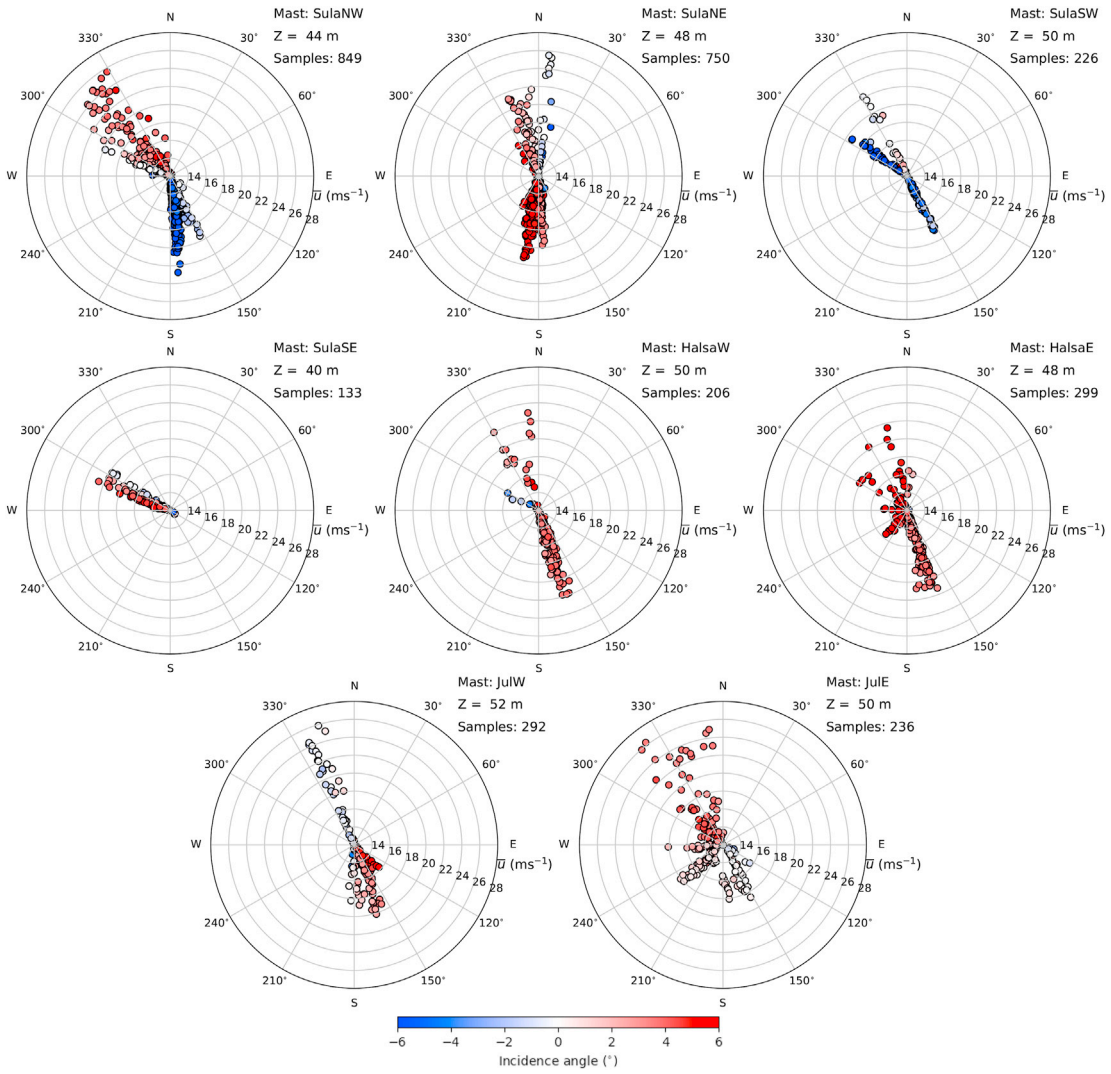

Fig. 6. Wind roses showing the mean wind velocity (u) and incidence angles (IA) recorded by the anemometers installed closest to 50 m above the ground at Sulafjorden, Halsajorden and Julsundet for the period 01-01-2018 to 31-12-2019.

Table 3
Incidence angle (IA): Location of met-mast, wind direction, median, 5th and 95th percentile. The results reported are given for the anemometer closest to 50 m above the ground.

Mast	Sector (°)	Median IA	5th percentile	95th percentile
SulaNW	135–165	−2.26	−3.60	−1.05
	165–185	−5.51	−6.77	−4.44
	300–330	3.45	2.54	4.34
SulaNE	300–20	1.59	−2.33	5.59
	150–210	5.11	2.60	6.99
SulaSW	135–165	−3.93	−6.63	−0.81
	285–315	−9.46	−11.21	−5.26
	315–345	0.92	−2.07	6.31
SulaSE	270–330	4.06	−0.61	7.80
HalsaW	150–180	3.53	2.54	4.26
	285–360	3.10	−3.39	8.63
HalsaE	150–180	3.54	2.52	4.41
	210–285	6.19	5.38	8.40
	300–360	7.70	5.70	8.46
JulW	120–195	3.15	0.06	5.68
	330–360	−0.41	−1.90	1.22
JulE	120–195	0.58	−0.71	1.59
	210–285	1.29	0.21	2.92
	300–360	3.79	3.18	4.70

corresponding wind roses for the anemometer nearest to 50 m above the ground level. The distributions are in general, positively skewed with a maximum in the probability density of 6 m s^{-1} or below. Most of the sites show a clear deviation from a Weibull type distribution typically observed in open and flat terrain. One typical feature is the strong over-representation of low wind speeds, in particular, visible for SulaNE, SulaSE, and HalsaE, indicating a reduction of wind speed by the influence of terrain and surrounding vegetation. Furthermore, the uneven directional distribution of the flow channelled inside the fjord might also lead to a deviation from the Weibull distribution.

The wind roses show, for $u \geq 12$ m s^{-1}, a limited number of directional sectors, emphasizing the channelling effect by the surrounding topography. These roses document also the complexity of the measurement setup by distinct and systematic differences across the different fjords and with different position inside the same fjord. For the three fjords investigated, the general flow pattern in 2018 and 2019 tends to be dominated by a wind from south and southeast to north and northwest. This is largely due to flow channelling caused by mountains on the east and west side of the respective fjords. At SulaNW and SulaNE, the most dominant wind directions correspond to a south-southeasterly and north-northwesterly flow. At SulaSE, the strongest winds come from the west-north-west whereas, at SulaSW, large velocities are recorded either for a north-westerly or southerly flow. The wind roses for Halsafjorden show

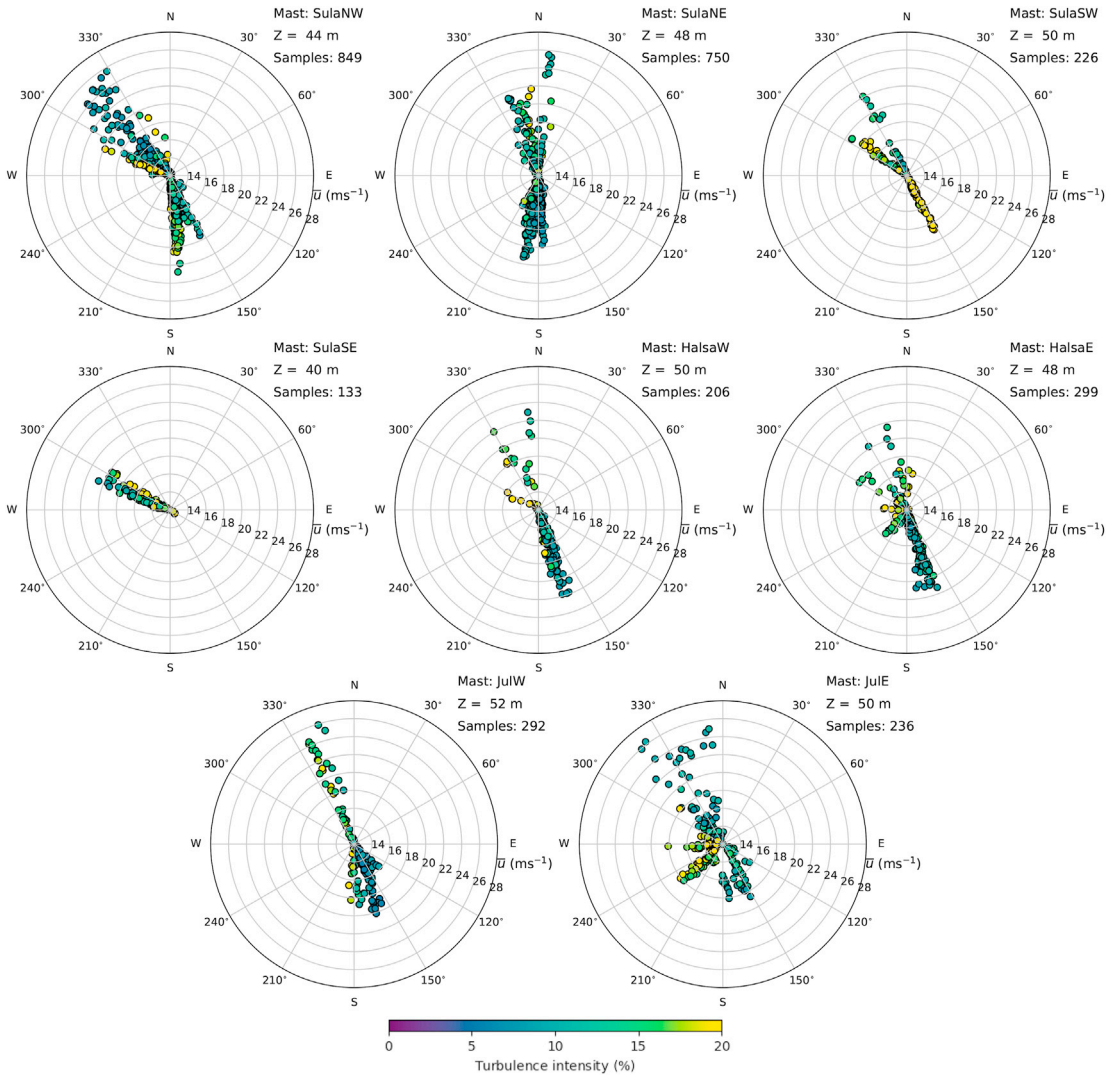

Fig. 7. Wind roses showing the mean wind velocity (u) and turbulence intensity (I_u) recorded on the anemometer installed closest to 50 m above the ground at Sulafjorden, Halsafjorden and Julsundet for the period 01-01-2018 to 31-12-2019.

that the flow is dominated by southerly winds at HalsaW while on the other side of the fjord, at HalsaE, there is a distinctly larger spread in the directional distribution. Also, the wind roses on both sides of Julsundet display clear discrepancies, with a southerly dominance of wind flow at JulW and a more homogeneous directional distribution for JulE.

As shown in Figs. 1 and 2, the lower mean wind speed values observed at JulW and JulE may be linked to the orientation of the fjord with respect to the direction of the strongest wind, which is from west to north-west, and the proximity of the masts to the flank of the surrounding mountains. However, the middle part of Julsundet is still fairly exposed to northern wind blowing from the sea. Complementary studies using wind tunnel tests or computational fluid dynamic simulations may help to assess the vulnerability of Julsundet to strong northern wind, but these are beyond the scope of this study.

The detailed data analysis is done hereafter for the sectors associated with the strong wind conditions only, i.e. one to three specific sectors per mast and that is because the flow characteristics vary significantly with the wind direction.

4.2. Flow horizontality

A major source of uncertainty in the design of a long-span bridge in complex terrain comes from the aerodynamic characteristics of the deck, which are functions of the incidence angle (Davenport, 1961a; Scanlan, 1978). Measuring incidence angles from in-situ sensors is also valuable to assess to what degree the terrain slopes affect the measurements by the sonic anemometers. Besides, strongly non-horizontal flows may be associated with flow separation phenomena, which challenge the traditional modelling of atmospheric boundary-layer turbulence.

Fig. 6 shows the mean incidence angle (IA) as a function of the wind direction while Table 3 summarises the mean IA recorded in terms of median and percentile values. The met-masts at JulW and JulE show flow conditions closest to horizontality compared to Sulafjorden and Halsafjorden. This is presumably due to the long fjord-fetch at these masts and the exposed locations on low headlands protruding into the water. As observed in Cheynet et al. (2018a), the flow follows the terrain slopes: positive IA indicates positive slopes upwind of the sensor whereas a negative IA reflects negative slopes.

The median values for Sulafjorden and Halsafjorden, range from −9.5° (SulaSW, sector 285°-315°) to 7.7° (HalsaE, sector 300°-360°) while some sectors show an almost horizontal flow (JulW, sector 330°-360°). The large variability observed in Table 3 reflects the diversity of the topographic elements around each mast.

At some of the stations, such as SulaNW or SulaSE, the wind roses indicate two different flow regimes within one relatively narrow sector. The local terrain around the masts is characterized by hills, trees, ridges

Table 4
Mean shear coefficient α and associated root-mean square value (RMSE), which were ensemble-averaged over N samples. Only wind velocity above 12 m s^{-1} at every height were considered. Data outside the 1st and 99th percentile were considered as outliers and removed.

Mast	Sector (°)	N	α	RMSE
SulaNW	135–165	125	0.02 ± 0.04	0.0024 ± 0.0028
	165–185	599	0.06 ± 0.03	0.0034 ± 0.0062
	300–330	275	0.02 ± 0.03	0.0094 ± 0.0163
SulaNE	330–20	203	0.04 ± 0.03	0.0082 ± 0.0131
	150–210	876	0.02 ± 0.04	0.0132 ± 0.0200
SulaSW	135–165	60	0.12 ± 0.06	0.0150 ± 0.0087
	285–315	40	0.08 ± 0.03	0.0243 ± 0.0085
	315–345	42	0.08 ± 0.02	0.0142 ± 0.0179
SulaSE	270–330	95	0.15 ± 0.05	0.0312 ± 0.0140
HalsaW	150–180	166	0.07 ± 0.03	0.0029 ± 0.0042
JulW	150–180	93	0.04 ± 0.02	0.0111 ± 0.0020
	330–360	84	0.08 ± 0.03	0.0090 ± 0.0034
JulE	210–270	60	0.09 ± 0.05	0.0063 ± 0.0066
	300–360	143	0.06 ± 0.01	0.0067 ± 0.0089

or escarpments which have a three-dimensional effect on the flow and has likely a major influence on the abrupt change of flow conditions. At SulaSW, the mast is located downstream of a gentle hill and a ridge, when the wind direction is 150° and 180°, respectively. The slopes of the ridge are much steeper than the slope of the hill, resulting in strongly negative mean incidence angles with values below −4°. On the other hand, the wind blowing from 150° is associated with an incidence angle around −2° or lower at a height of 44 m above the surface. A similar situation is observed at SulaSW for the sector 300°-330°.

At SulaNE, the northern sector reflects an up-slope flow coming from the sea when the wind direction is 330°, whereas the wind direction around 0° is associated with a downslope flow brushing against the mountain's flank. Although a wind direction around 300° at SulaSE corresponds to a limited number of storms in 2018–2019, similar observations were done at lower wind speeds. The strongly positive incidence angles are likely due to the presence of an escarpment, ca. 110 m to the northwest to the mast, followed by a positive slope. The southern side of the escarpment is free from any vegetation and limited by the sea, whereas the northern side is covered by bushes and small trees. The larger turbulence intensity in Fig. 7 at SulaSE for a wind direction slightly larger than 300° can be attributed to this vegetation, which locally increases the roughness length. Morse et al. (2002) showed that a forest edge can also significantly affect the mean incidence angle. Therefore, it is possible that the nearly horizontal flow observed at SulaSE for a mean wind direction slightly above 300° is a consequence of the flow passing over the trees located on the northern side of the ridge.

At Sulafjorden and Halsafjorden, a mean absolute incident angle up to 9° is recorded (Table 3), which is substantively larger than values reported from anemometers mounted above the deck of suspension bridges (Fenerci and Øiseth, 2017; Cheynet et al., 2019). Kristensen and Jensen (1979) measured an incidence angle up to 7° on the Sotra bridge, but their measurements were affected by deck-induced flow distortion (Kristensen and Jensen, 1979; Cheynet et al., 2019). Sonic anemometer measurements from masts installed in Bjørnafjorden (Cheynet et al., 2018a) showed angles of attack that were also up to 6° at $u > 12$ m s^{-1}.

While the flow is expected to be more horizontal near the middle of the fjord than on its sides, the measured incidence angles are still valuable as they could be used to validate CFD models, which would aim to quantify the incidence angles along the deck of a fjord-crossing bridge. It should also be noted that a large incidence angle leads to a non-linear dynamic response that can be significant (Argentini et al., 2020; Diana et al., 2010; Diana and Omarini, 2020). Therefore, overestimating the incidence angle is not desirable from a design perspective.

4.3. Mean wind shear

The local terrain does not only affect the incidence angle but also the mean wind shear, which is quantified hereafter, for each selected sector, using the power-law coefficient (Frost, 1948) also called shear coefficient in the following. This coefficient is estimated by fitting the wind profile power law to the mean wind speed profile estimated on each mast using three or four sensors, when available. The power coefficient α is here used to supplement the incidence angle to describe the local topographic effects on the estimated flow characteristics. The calculated shear coefficients are shown in Table 4, which includes the root mean square error between the fitted and measured mean wind speed values. Cases in which the wind speed at all elevations is lower than 12 m s^{-1} have been ignored which resulted in no computation of the shear coefficient for HalsaE as well as for the winds coming from the south at JulE.

The wind speed profile depends on the terrain and the thermal stratification of the atmosphere (Touma, 1977; Irwin, 1979; Monin and Obukhov, 1954). Selecting high wind speeds does not guarantee neutral stability conditions but reduces the occurrence of records characterized by a stable and unstable thermal stratification of the atmosphere. Thus, the shear coefficient for a given wind sector will mainly be determined by the local topography.

The shear coefficients are ensemble-averaged for each of the directional sectors selected. For every sector at SulaNW, SulaNE, HalsaW, JulW, and JulE, a small mean shear is obtained, with $\alpha \leq 0.09$. The largest shear coefficients are obtained at SulaSW and SulaSE with values of 0.12 and 0.15, respectively. The standard deviation associated with these shear coefficients shows that the α values found may not be significantly different in most of the masts and sectors considered. Hsu et al. (1994) report an average shear coefficient of 0.11 for wind over the ocean, whereas Tamura et al. (2007) measured 0.10 for wind from the sea and 0.20 to 0.30 for wind over land for wind speed between 12 m s^{-1} and 16 m s^{-1}. The low values of the shear coefficients observed suggest possible speed-up of the flow by hills immediately upstream of the masts or at the mast location itself (Ishihara et al., 1999; Jackson and Hunt, 1975). Accordingly, the values $\alpha \geq 0.12$ observed at SulaSE and SulaSW are linked to the wind blowing over a long fetch above the sea with limited disturbance from the terrain upstream of the masts.

4.4. Flow Gaussianity

The peak response of a structure to a non-Gaussian dynamic load can be much larger than in the case of a Gaussian distribution (Karmakar et al., 2012; Kareem et al., 1998). Therefore, assessing the flow Gaussianity is valuable to model properly the extreme wind load (Gurley and Kareem, 1997). Besides, if a random process is Gaussian, it can be described using the first two statistical moments only, which is attractive for modelling purposes.

For the sectors selected, Fig. 8 shows that the along-wind component is generally Gaussian while it is not the case for the vertical component. However, for the case of HalsaW sector 285°-360° and JulE sector 210°-285°, at measurement height located below 15 m above the ground and near the vegetation cover, the skewness of the along-wind component is considerable indicating non-Gaussian characteristics. Similar observations were done by Fernández-Cabán and Masters (2017); Yuan and Jouybari (2018). The skewness of the u component is not expected to differ substantially between flat and complex terrain, whereas the excess coefficient may increase (Mahrt, 2011). There are some few situations where the excess coefficient κ_u is significantly different from zero: At SulaSW for a wind direction between 135° and 165° and JulW for a wind direction between 330° and 360°. In both cases, the flow is associated with a slightly negative incidence angle (IA) with a value down to −2° and a wind direction almost parallel to the coast. This implies that multiple roughness changes are likely occurring, which could modify the distribution of the along-wind component u.

The distribution of the cross-wind component v is not always

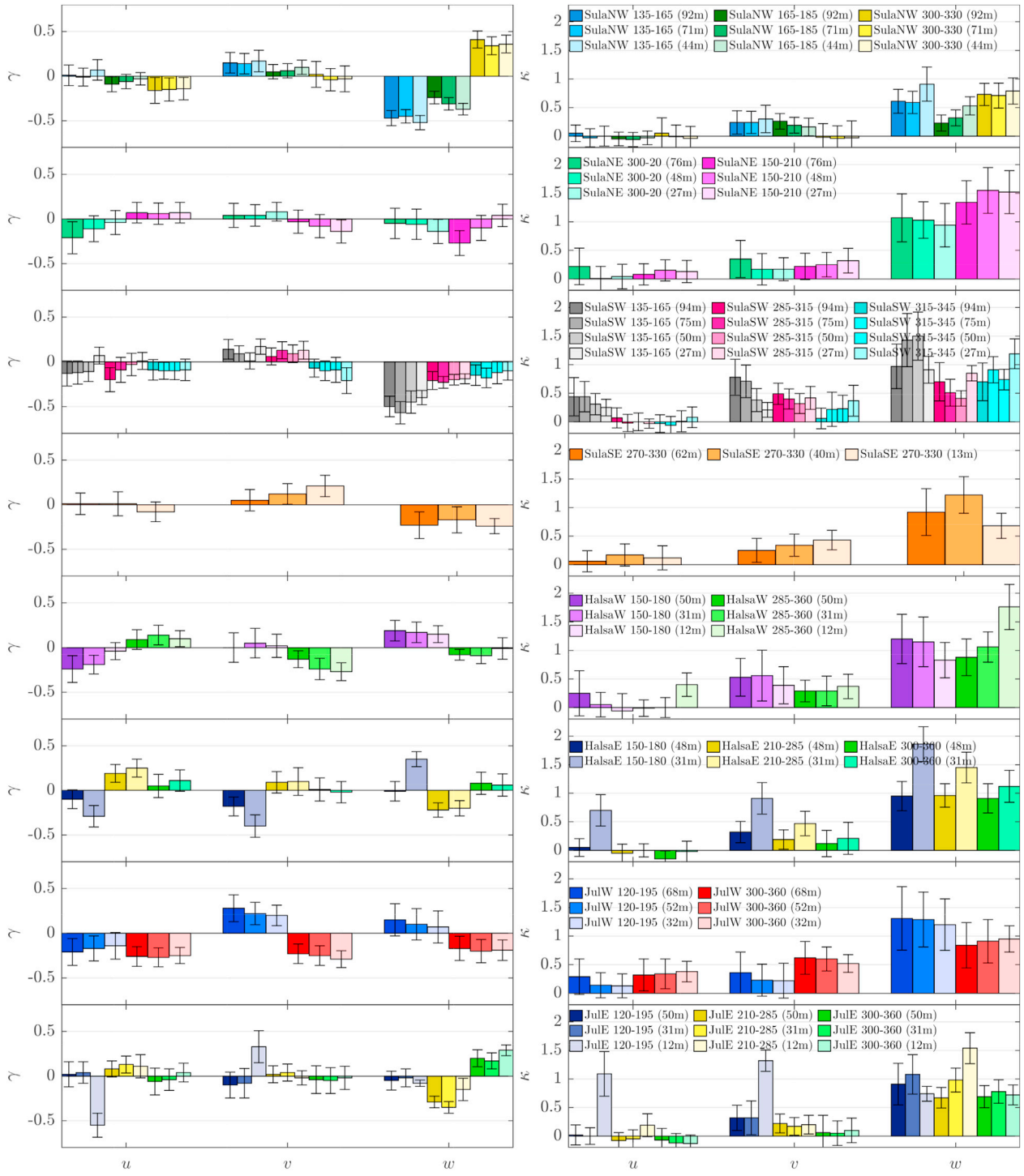

Fig. 8. Skewness γ and excess coefficient κ at the met-masts at Sulafjorden, Halsafjorden and Julsundet with $u \geq 12$ m s^{-1} at all heights. Data outside the 1st and 99th percentile were considered as outliers and removed. The error bar represents one standard deviation. A more detailed summary is available in Table 7.

Gaussian and varies strongly with the sector selected. It can be noted that flow measurements at heights below 30 m in forested areas should be interpreted with care, as they may be affected by the vegetation. The cross-wind component v has an excess coefficient κ_v below 0.3 if the anemometers are not at the feet of a mountain and if the wind is blowing over a long fetch of water, for example at SulaNW, JulE, and HalsaE for a northwesterly flow and JulW for a northeasterly flow. In most of the other cases, the cross-wind component v has a non-negligible excess coefficient.

In the present case, a horizontal flow does not imply that the fluctuations are Gaussian. This is particularly visible for the vertical wind component w. At a height of 50 m above ground at SulaSW and JulW, the two sectors associated with a nearly horizontal flow correspond to a wind direction of ca. 330°. For both sectors, the excess coefficient of the vertical wind component w is above 0.7 whereas the skewness is close to zero. Sectors with IAs below −4° (SulaNW, and SulaSW) shows the most Gaussian fluctuations for the vertical components with $\kappa_w < 0.5$ at most of the heights. Sectors with IAs above 4° (SulaNE, SulaSE, HalsaE, HalsaW, and JulW) shows in most of the cases $\kappa_w > 1$.

It cannot be deducted from the mast measurements on the seaside

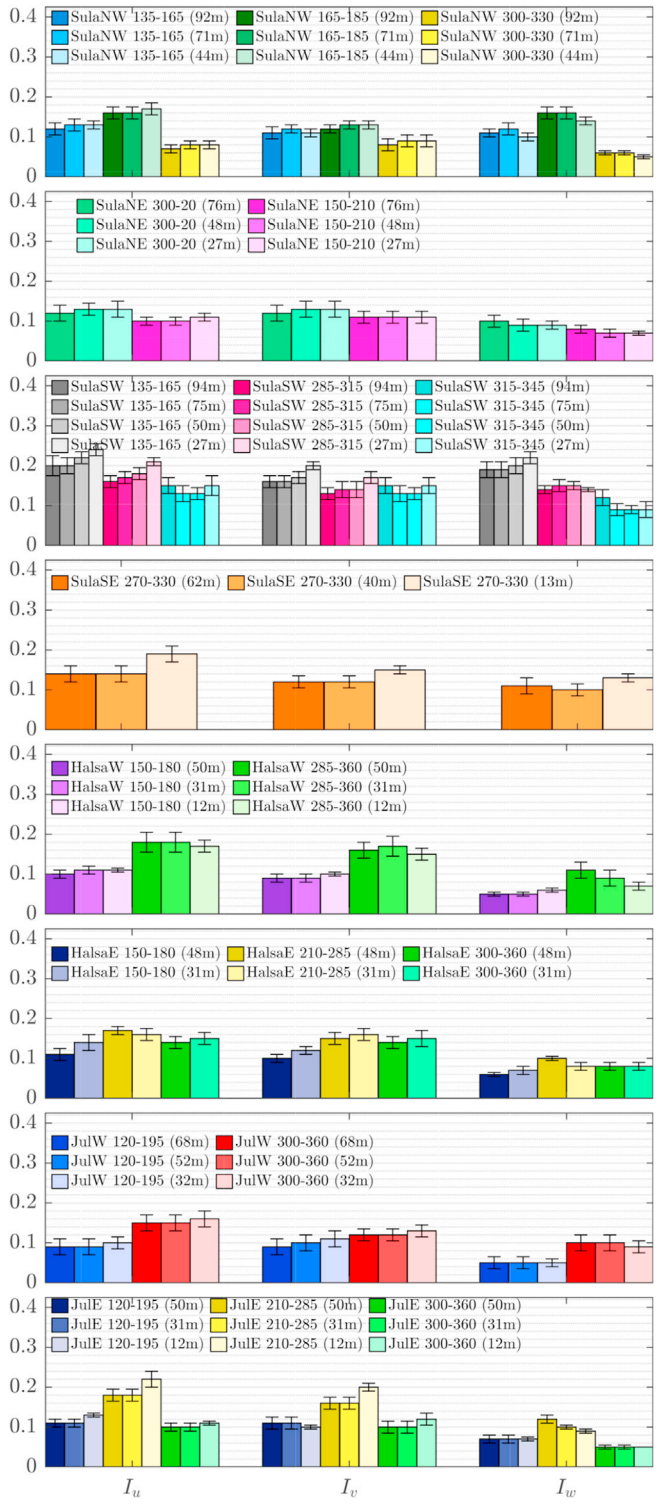

Fig. 9. Turbulence intensity of the three velocity components at the met-masts in Sulafjorden, Halsafjorden and Julsundet with $u \geq 12$ m s^{-1} at every height. Data outside the 1st and 99th percentile were considered as outliers and removed. The error bar represents one standard deviation. A more detailed summary is available in Table 8.

whether the vertical velocity component has a non-Gaussian distribution over the whole width of the fjord. Yet, this should be clarified as the vertical wind speed component governs the vertical and torsional buffeting response of long-span bridges.

Table 5
Normalized standard deviation at Sulafjorden, Halsafjorden and Julsundet, for $u > 12$ m s^{-1} at every height and at a sector with a long-fetch winds. The anemometers closest to 50 m above ground is chosen.

Mast	Sector (°)	σ_w/u_*	σ_v/u_*	σ_u/u_*	σ_w/σ_u	σ_v/σ_u
SulaNW	300–330	1.41 ± 0.19	2.39 ± 0.56	2.09 ± 0.38	0.68 ± 0.10	1.15 ± 0.24
	135–165	1.97 ± 0.34	2.37 ± 0.42	2.62 ± 0.51	0.76 ± 0.09	0.92 ± 0.14
SulaNE	150–210	1.76 ± 0.30	2.81 ± 0.56	2.65 ± 0.51	0.67 ± 0.09	1.07 ± 0.17
	300–20	1.71 ± 0.33	2.35 ± 0.71	2.40 ± 0.52	0.72 ± 0.10	0.97 ± 0.17
HalsaW	150–180	1.42 ± 0.20	2.32 ± 0.42	2.64 ± 0.43	0.54 ± 0.06	0.88 ± 0.12
HalsaE	150–180	1.57 ± 0.29	2.61 ± 0.52	2.91 ± 0.62	0.55 ± 0.05	0.91 ± 0.11
	300–360	1.39 ± 0.27	2.45 ± 0.48	2.55 ± 0.58	0.56 ± 0.08	0.98 ± 0.16
JulW	120–195	1.46 ± 0.29	2.76 ± 0.53	2.62 ± 0.65	0.57 ± 0.10	1.08 ± 0.20
JulE	120–195	1.65 ± 0.27	2.65 ± 0.68	2.74 ± 0.55	0.61 ± 0.11	0.97 ± 0.17
	300–360	1.21 ± 0.13	2.32 ± 0.59	2.25 ± 0.40	0.55 ± 0.08	1.04 ± 0.22

Table 6
Normalized standard deviation at Sulafjorden, Halsafjorden and Julsundet, for $u > 12$ m s^{-1} at every height for short-fetch winds. The anemometers closest to 50 m above ground is chosen.

Mast	Sector (°)	σ_w/u_*	σ_v/u_*	σ_u/u_*	σ_w/σ_u	σ_v/σ_u
SulaNW	165–185	1.98 ± 0.33	1.83 ± 0.35	2.32 ± 0.42	0.85 ± 0.07	0.79 ± 0.07
SulaSW	135–165	1.68 ± 0.24	1.44 ± 0.12	1.81 ± 0.17	0.93 ± 0.12	0.80 ± 0.09
	285–315	1.77 ± 0.24	1.72 ± 0.33	2.19 ± 0.27	0.81 ± 0.07	0.79 ± 0.15
SulaSE	270–330	1.47 ± 0.23	1.96 ± 0.42	2.16 ± 0.38	0.69 ± 0.09	0.92 ± 0.18
HalsaW	285–360	1.52 ± 0.26	2.43 ± 0.70	2.74 ± 0.74	0.57 ± 0.08	0.89 ± 0.12
HalsaE	210–285	1.52 ± 0.17	2.41 ± 0.31	2.61 ± 0.27	0.59 ± 0.05	0.93 ± 0.10
JulW	330–360	1.58 ± 0.23	2.04 ± 0.48	2.51 ± 0.35	0.63 ± 0.08	0.81 ± 0.12
JulE	210–285	1.80 ± 0.32	2.44 ± 0.47	2.84 ± 0.49	0.64 ± 0.05	0.86 ± 0.09

4.5. Single point turbulence characteristics

4.5.1. Turbulence intensity

The turbulence intensity here defined as the ratio of the standard deviation of the velocity component with mean wind speed is given in Fig. 7, which shows the dependency of I_u on the wind direction for the different masts. The sector-averaged *TI* estimates, at various sensor heights, together with the corresponding standard deviations, are summarised in Fig. 9. For sectors where the flow is relatively unaffected by the local terrain and has a long fetch over open water, e.g. the northwest of SulaNW and south of SulaNE, the average *TIs* ($I_u/I_v/I_w$) are 0.08/0.09/0.06 and 0.10/0.11/0.08, respectively. In Halsafjorden the average *TIs* for the southern sector of HalsaW and HalsaE are 0.10/0.09/0.05 and 0.11/0.10/0.06. At Julsundet, south of JulW, the *TIs* are 0.09/0.09/0.05 while the south and northwest of JulE the *TIs* are 0.11/0.11/0.07 and 0.10/0.10/0.05.

A turbulence intensity between 0.08 and 0.10 at a height of 50 m above ground is typically observed in coastal regions when the wind is blowing over a long fetch or offshore under strong wind conditions. In the Eurocode (EN 1991-1-4, 2005), if the turbulence factor and

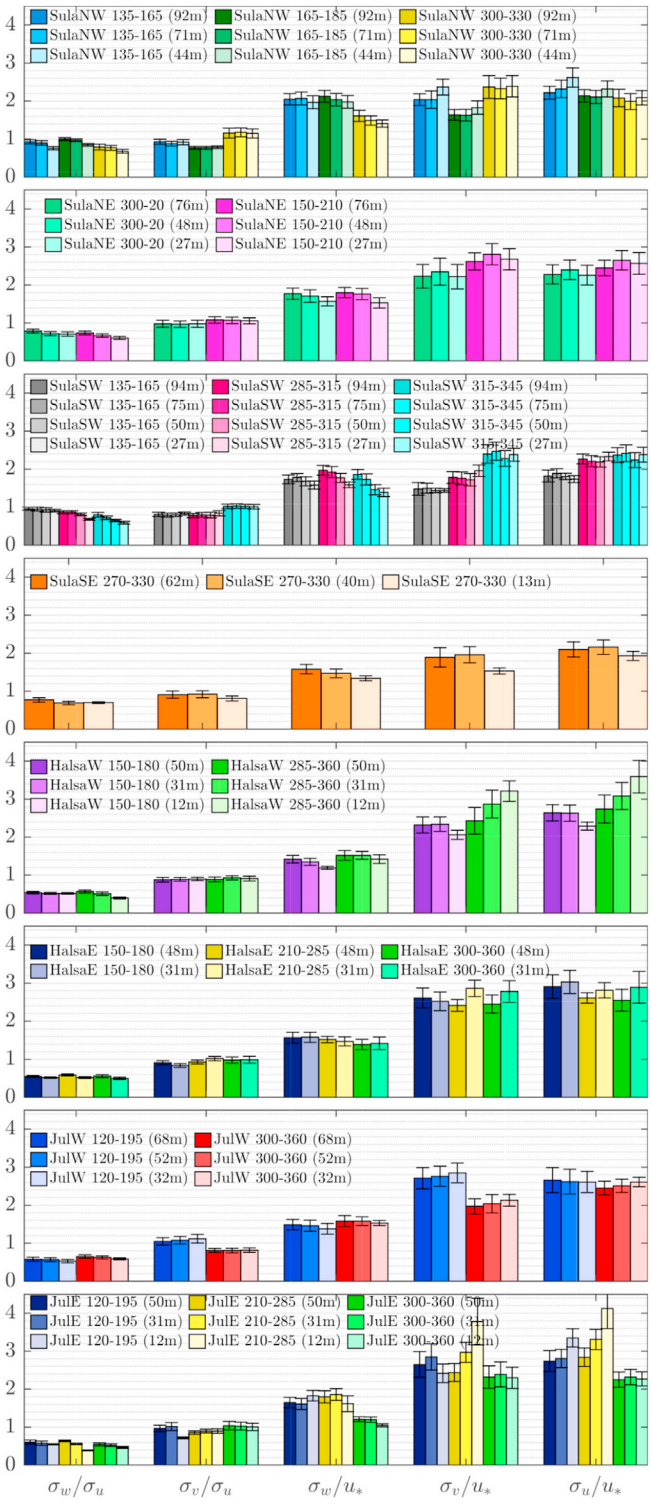

Fig. 10. Normalized standard deviation of the three velocity components at the met-masts located in Sulafjorden, Halsafjorden and Julsundet with $u \geq 12$ m s^{-1} at every height. Data outside the 1st and 99th percentile were considered as outliers and removed.The error bar represents one standard deviation. A more detailed summary is available in Table 9.

topography factor are both set equal to one, $I_u(z = 50\text{ m}) = 0.10$ corresponds to a terrain category 0, for which the roughness length z_0 is 0.003 m. It should be noted that the value $z_0 := 0.003$ m is primarily used for the calculation of the design wind load, which is the reason it is much higher than the roughness length usually measured for a calm sea, which is around 0.0002 m (Wieringa, 1992). Interestingly, similar turbulence intensities were observed in Bjørnafjorden (Cheynet et al., 2018a) and on the Sotra Bridge (Kristensen and Jensen, 1979) for similar wind conditions and a long fetch, which confirms that turbulence characteristics in Norwegian fjords may share common features.

If the terrain upwind to the masts is more complex, e.g. for southerly flow at SulaNW, a southeasterly flow at SulaSW or a northwesterly flow at SulaSE, much higher *TI*s are measured. The corresponding values ($I_u/I_v/I_w$) are 0.16/0.13/0.16, 0.22/0.17/0.20 and 0.14/0.12/0.11 at SulaNW, SulaSW and SulaSE, respectively. Similarly, for the northwesterly sector of HalsaW, western sector of HalsaE, northwest of JulW and west of JulE, the *TI*s are 0.18/0.16/0.11, 0.17/0.15/0.10, 0.15/0.12/0.10, and 0.18/0.16/0.12, respectively. The average values of *TI*s in these directions are consistent with those reported by Harstveit (1996). The large values of I_u, between 0.14 and 0.22, observed when the flow is passing over irregular terrains, is also expected and is remarkably close to values observed from the Hardanger Bridge (Lystad et al., 2018) and the Lysefjord Bridge (Cheynet et al., 2019). Although the wind measurements in Sulafjorden, Halsafjorden and Julsundet are strongly affected by the local topography, the similarities of the values of the turbulence intensities among the three locations as well as with previous studies confirm the relevance of the measurement data for the design of the planned fjord crossings.

4.5.2. Normalized standard deviation

The sector-averaged single-point turbulence statistics and their associated standard deviation are reported for two different cases: (a) For winds coming from directions considered to have long fjord fetch upstream, denoted herein as long-fetch winds (Table 5); (b) for winds coming from directions considered to have an irregular topography upstream of the mast referred to as short-fetch winds (Table 6). The values of σ_w/u_* are typically in the range of 1.2–1.3 for flat and uniform terrain under neutral conditions (Kaimal and Finnigan, 1994) but can significantly differ from these values in a mountainous environment (de Franceschi et al., 2009). On the Sotra Bridge, Jensen & Hjort-Hansen (1977) estimated $\sigma_w/u_* \approx 1.5$, whereas values ranging from 1.4 to 1.8 were recorded on the Lysefjord Bridge (Cheynet et al., 2019). The values of σ_w/u_* found in the present studies range also from 1.2 to 1.8 when the wind is blowing over a long fetch. However, for short-fetch winds σ_w/u_* ranges from 1.5 to 2.0. The large scatter observed for the ratio σ_w/u_* is, therefore, linked to the different terrain characteristics at the masts.

The values of σ_u/u_* and σ_v/u_* are challenging to interpret because of the scatter observed. The horizontal turbulence components are more affected by topographical features than the vertical component. Under neutral conditions, the horizontal velocity spectrum contains low-frequency eddies with more energy than the vertical velocity spectrum (Panofsky et al., 1982). This low-frequency range is more easily disturbed by hills and roughness changes than the high-frequency range (Frank, 1996; Mann, 2000). Therefore, σ_u/u_* and σ_v/u_* are expected to show an increasing range of values in rough terrain compared to the case of flat terrain. For examples, $\sigma_u/u_* > 2.6$ and $\sigma_v/u_* > 2.0$ are expected in rolling terrain (de Franceschi et al., 2009). In the present case, table 9 shows values consistent with those recorded at the inlet of a narrow fjord (Cheynet et al., 2019). However, lower-than-expected values of σ_u/u_* are also found in Fig. 10. These might be associated with a flow along the mountain slopes.

In flat and homogeneous terrain, a ratio $\sigma_w/\sigma_u \approx 0.5$ is expected (Solari and Piccardo, 2001). This value is also used in the Handbook N400 (Norwegian Public Road Administration, 2015), which is used for the design of suspension-bridges in Norway. The turbulence model by Kaimal et al. (1972), with correction in the inertial sub-range, leads to a ratio $\sigma_w/\sigma_u = 0.57$ (Kaimal and Finnigan, 1994). Offshore wind measurements conducted 80 m above the surface for neutral conditions provided $\sigma_w/\sigma_u = 0.53$ (Cheynet et al., 2017a). In the present study, the ratio σ_w/σ_u is around or above 0.6 for every anemometer at a height close to or equal to 50 m above the ground. Such values are consistent with

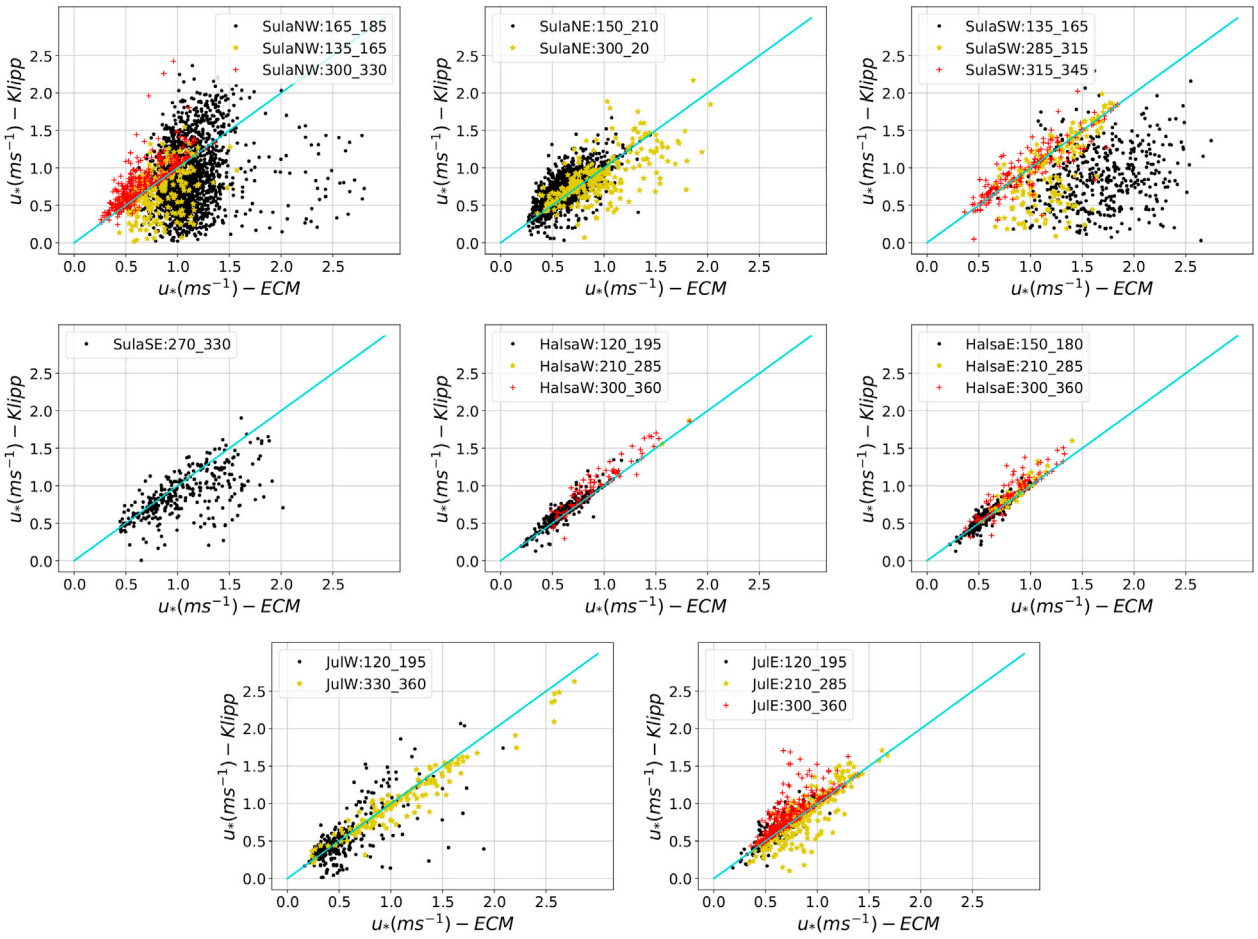

Fig. 11. Friction velocity calculated with the eddy-covariance method (ECM, eq. (5)) and Klipp's method using data collected by the anemometer closest to 50 m above the ground at each mast between the 01-01-2018 to 31-12-2019.

previous records from fjord-crossing bridges (Jensen and Hjort-Hansen, 1977; Cheynet et al., 2019) or masts on the shores of Bjørnafjorden (Cheynet et al., 2018a). Cheynet et al. (2019) argued that the failure to account for the unusually high value of σ_w/σ_u in a fjord leads to a substantial underestimation of the vertical buffeting response of a long-span suspension bridge.

A ratio $\sigma_w/\sigma_u > 0.8$ is unusually large but has been reported in a few case studies in fjords (Øiseth et al., 2013). In the present case, $\sigma_w/\sigma_u > 0.8$ might be linked to specific wind directions combined with the proximity of the anemometers being at the flanks of mountains. Providing that the flow is following Sulafjorden, it is unlikely that the value σ_w/σ_u is above 0.8 in the middle of this fjord. In Halsafjorden, the ratio σ_w/σ_u is between 0.50 and 0.60 for the different sectors selected. This indicates that in this fjord, the flow characteristics on the shore might be closer to the case of a flat terrain than at Julsundet or Sulafjorden. In table 9, the ratio σ_w/σ_u is below or equal to 0.5 when the anemometers are located 12 m above the ground, which testifies for local flow distortion by the surrounding trees. It should be noted that the ratio $\sigma_w/\sigma_u \approx 0.4$ recorded on the Hardanger bridge (Fenerci and Øiseth, 2018b) is slightly lower than reported in the other Norwegian fjords. It is unsure whether it is due to flow-distortion by the deck, sensor calibration error (Gill Instruments, 2016; Billesbach et al., 2019), or simply peculiar flow characteristics at the bridge location.

The ratio σ_v/σ_u is expected to range from 0.7 to 0.9 in flat terrain (Solari and Piccardo, 2001). The ratio σ_v/σ_u in the Kaimal model is 0.76. In an offshore environment, 80 m above the surface, Cheynet et al. (2019) reported a ratio equal to 0.77. In the present study, the ratio σ_v/σ_u ranges from 0.7 to 1.2 for the different fjords. It appears that ratios close to or larger than one occur when the mountain's flanks are close to the anemometers, which may have a blocking effect and important directional shear, visible in the Reynolds stress tensor. Overall, the values found on the seaside are consistent with the measurement from fjord-crossing bridges (Jensen and Hjort-Hansen, 1977; Cheynet et al., 2019; Øiseth et al., 2013), except the Hardanger bridge (Fenerci and Øiseth, 2018b), where $\sigma_v/\sigma_u \approx 0.15$, which might not be realistic.

4.5.3. Friction velocity

The reader is reminded that the friction velocity is the fundamental velocity in surface layer scaling (Kaimal and Finnigan, 1994). Besides, it conveniently links the logarithmic wind speed profile with the velocity spectra for wind load modelling. The value of friction velocity depends also on the tilt correction algorithm used. As pointed out by Klipp (2018) or Wilczak et al. (2001), a sectoral planar fit method may not be appropriate in terrain where flow separation occurs, which is likely the case at the mast locations.

In Fig. 11, the friction velocity computed using eq. (5) is compared with the method by Klipp (2018). In flat terrain and neutral atmosphere, both approaches to compute u_* should yield similar results. On the other hand, discrepancies are expected in the presence of steep mountains slopes. To assess the influence of $v'w'$ and $u'v'$ on the friction velocity computed with Klipp's method, correlated wind velocity histories were simulated with non-zero covariance between the three velocity components. The simulated time series showed that $v'w'$ and $u'v'$ have some influence on the computation of the friction velocity, but these were more limited than observed in Fig. 11. Therefore, $v'w'$ and $u'v'$ may not explain the observed discrepancies, alone, especially if the atmospheric

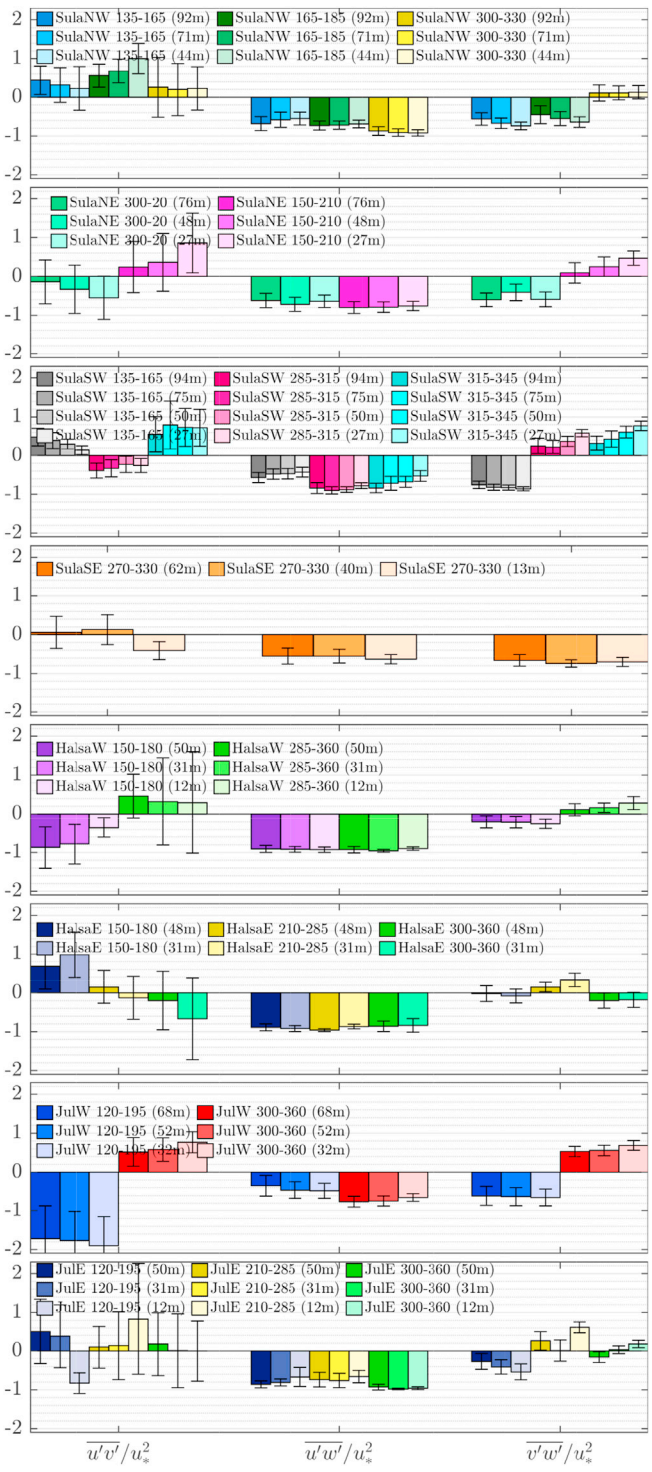

Fig. 12. Turbulent momentum fluxes at the met-masts at Sulafjorden, Halsafjorden and Julsundet with $u \geq 12$ m s^{-1} at every height. Data outside the 1st and 99th percentile were considered as outliers and removed. The error bar represents one standard deviation. A more detailed summary is available in Table 10.

stratification is non-neutral. Although velocity records above 12 m s^{-1} were used, the data set likely includes some samples representative of unstable or stable conditions, especially near the coastline.

As shown in Figs. 11 and 12, the friction velocity estimated at Halsafjorden using either Klipp's method or eq. (5) are in good agreement, even though $u'v'/u_*^2$ can have the same magnitude as $u'w'/u_*^2$. In Halsafjorden, the term $v'w'/u_*^2$ is close to zero while this is not the case for the masts at Sulafjorden and Julsundet, where the mountains are steeper and higher than at Halsafjorden. One exception is observed at Sulafjorden, for which $v'w'/u_*^2$ is small when the wind is blowing from northwest, the reason for this is, however, unclear. Nevertheless, the study of momentum fluxes helps to better understand the influence of topography on the measurements.

5. Conclusions

The paper explores a subset of a larger data set aiming to identify the wind conditions relevant for bridge design at three potential fjord-crossing sites, in complex coastal terrain, in western Norway. Two years of continuous wind measurements were analysed, at heights between 12 m and 95 m above the ground, in masts located on the shore of the three fjords Sulafjorden, Julsundet and Halsafjorden. Eight masts were considered for the analysis, each of them instrumented with three to four sonic anemometers, i.e., 25 sonic 3D anemometers in total.

To focus on strong wind conditions of particular relevance for bridge design, only samples with a mean wind speed above 12 m s^{-1} were selected. The goal was to quantify to what extend the local topography affects the flow conditions recorded at the shoreline by the anemometers and how met-masts can be used to collect and provide correspondingly filtered data valuable for bridge-design. The study highlighted also some challenges associated with flow characterization near mountain slopes, especially for the design of wind-sensitive structures. The main findings of the study are as follows

- Many of the masts are in sheltered locations where weak winds are predominant. Wind speeds above 12 m s^{-1} are uncommon at several of the sites during the period analysed. This implies that several years of data are required to capture a sufficient amount of strong wind conditions, critical for the relevant bridge design.
- The flow on the shore of the fjords is horizontal for a limited number of situations only. A median incidence angle up to $-9.5°$ was measured at Sulafjorden. In Halsafjorden and Julsundet, values up to 7.7° and 3.8° were observed. For the majority of the directional sectors considered, the mean wind speed profiles fitted by the wind profile power law provided shear coefficients below 0.10. A low mean wind shear may reflect the flow speed-up above the hills. Such observations indicated that, on several occasions, the sensors were likely inside the internal boundary layers created by the rough terrain upstream of the masts.
- Significant deviations from the assumption of Gaussian fluctuations were observed. The non-Gaussianity was assessed using the skewness and excess kurtosis. Non-Gaussian fluctuations were particularly strong in the vertical velocity component whereas the along-wind component was generally Gaussian, except when the flow was distorted by the surrounding vegetation. The influence of the terrain upwind to the masts on the skewness and excess kurtosis was significant, especially for the lateral velocity component, at heights below 15 m and in the roughness sublayer. Finally, it was found that a horizontal flow does not imply Gaussian fluctuations on the shore of a fjord.
- The turbulence intensity showed a clear dependency on the sector selected. For sectors characterized by a large fjord fetch, the ensemble-averaged values for the turbulence intensities were up to 0.11 for the horizontal components and up to 0.08 for the vertical component. For the sector characterized by complex upstream topography, much larger values were measured with I_u, I_v and I_w up to 0.22, 0.17, and 0.20, respectively. These observations highlight the importance of studying sectorial differences of the wind conditions at the masts and for bridge design.
- The normalized standard deviation σ_w/σ_u and σ_v/σ_u were close to the values previously reported in the literature in Norwegian fjords. In the present case, σ_w/σ_u was around or above 0.6. While σ_v/σ_u ranged

from 0.7 to 1.2. These values are larger than advised in the handbook N400, used for the design of long-span suspension bridges in Norway. The ratio of the vertical standard deviation with the friction velocity σ_w/u_* showed a clear dependency on the wind sector chosen, ranging from 1.2 to 1.8 for long-fetch winds and from 1.5 to 2.0 when passing over complex terrain.

- Two methods to compute the friction velocity were assessed. Results suggested that at Halsafjorden, the turbulence measurements were less affected by the surrounding mountains than in Sulafjorden. Nevertheless, it is still unsure whether the friction velocity u_* computed with Klipp's method given in eq. (6) or the traditional double-rotation technique and eq. (5) should be used. Studies including an analysis of the Reynolds stress in complex terrain are scarce and often linked to boundary-layer micrometeorology. Therefore, it is legitimate to wonder if and how $u'v'$ and $v'w'$ should be accounted for in wind load modelling on structures.

The mast measurements near the shore of Sulafjorden, Halsafjorden and Julsundet provided valuable information on the local wind conditions. However, the aforementioned results suggest that the integral turbulence characteristics recorded on the seaside may not be representative of the flow conditions in the middle of the fjord. Therefore, to estimate the turbulent load acting on the deck of a fjord-crossing bridge with higher confidence, computational fluid dynamic (CFD) simulations or remote sensing observations of the flow field may be required to complement these anemometers records.

The integral flow characteristics provide only a partial understanding of the local flow conditions because turbulence covers a large range of wavenumbers or frequencies. The blocking by the surface distorts more easily large eddies, which are associated with low wavenumbers, than smaller eddies (Hunt and Morrison, 2000; Hunt and Carlotti, 2001; Högström et al., 2002). Also, the low-frequency range of the turbulence spectrum can be substantially affected by roughness changes and hills (Mann, 2000; Frank, 1996). The detailed assessment of the turbulence characteristics on the shores of fjords can be achieved through spectral analysis, providing that the velocity records can be described as stationary, ergodic random processes.

Therefore, the second part of the present study will focus on the spectral energy content of the velocity fluctuations. The one-point power spectral density can be used to indicate which frequency range is no-longer affected by the local topography and whether such a range has similar characteristics to traditional velocity spectra (Kaimal et al., 1972). The adequacy of computation of the friction velocity with Klipp's method (Klipp, 2018) will also be assessed in terms of normalization of the velocity spectra. This will help to investigate to what degree such a normalization follows surface-layer scaling in fjords. Two-point spectral densities will be studied through the coherence function. In particular, the blocking by the surface could substantially affect the vertical coherence such that Bowen's scaling (Bowen et al., 1983; Cheynet, 2019) may become more appropriate than Davenport's scaling (Davenport, 1961b) for the design and construction of the bridge towers.

CRediT authorship contribution statement

Zakari Midjiyawa: Conceptualization, Methodology, Software, Validation, Formal analysis, Investigation, Data curation, Writing – original draft, Writing – review & editing, Visualization. **Etienne Cheynet:** Conceptualization, Methodology, Software, Validation, Formal analysis, Investigation, Supervision, Writing – original draft, Writing – review & editing. **Joachim Reuder:** Conceptualization, Supervision, Writing – review & editing. **Hálfdán Ágústsson:** Writing – review & editing. **Trond Kvamsdal:** Supervision, Project administration, Writing – review & editing.

Declaration of competing interest

The authors declare that they have no known competing financial interests or personal relationships that could have appeared to influence the work reported in this paper.

Acknowledgements

This work and the measurement campaign is financed by the Norwegian Public Roads Administration as part of the Coastal Highway E39 project in Mid-Norway. We also want to thank Birgitte R. Furevik, Jørn Kristiansen and Knut Helge Midtbø (Norwegian Meteorological Institute), Konstantinos Christakos (University of Bergen), and Adil Rasheed (Norwegian University of Science and Technology) for providing resources and guidance necessary for this work.

Appendix

Table 7
Flow Gaussianity: Wind direction, height above terrain (H), number of samples (N), skewness γ, excess coefficient κ and associated standard deviation at the met-masts at Sulafjorden, Halsafjorden and Julsundet. Wind velocity above 12 m s^{-1} for all elevations. Data outside the 1st and 99th percentile were considered as outliers and removed.

Mast	Sector (°)	H	N	γ_u	γ_v	γ_w	κ_u	κ_v	κ_w
SulaNW	135–165	92	64	0.01 ± 0.23	0.15 ± 0.23	−0.47 ± 0.17	0.05 ± 0.29	0.24 ± 0.41	0.61 ± 0.42
		71	100	−0.01 ± 0.20	0.14 ± 0.23	−0.45 ± 0.15	−0.03 ± 0.32	0.24 ± 0.39	0.59 ± 0.39
		44	69	0.07 ± 0.23	0.17 ± 0.24	−0.52 ± 0.16	0.00 ± 0.35	0.30 ± 0.48	0.91 ± 0.60
	165–185	92	537	−0.09 ± 0.17	0.05 ± 0.16	−0.24 ± 0.14	−0.05 ± 0.24	0.26 ± 0.27	0.23 ± 0.28
		71	522	−0.06 ± 0.16	0.06 ± 0.16	−0.31 ± 0.14	−0.06 ± 0.25	0.19 ± 0.28	0.32 ± 0.28
		44	519	−0.03 ± 0.14	0.10 ± 0.16	−0.37 ± 0.13	−0.03 ± 0.24	0.16 ± 0.31	0.53 ± 0.32
	300–330	92	96	−0.16 ± 0.29	0.02 ± 0.29	0.41 ± 0.19	0.05 ± 0.54	−0.02 ± 0.48	0.73 ± 0.39
		71	87	−0.15 ± 0.26	−0.04 ± 0.25	0.34 ± 0.20	−0.01 ± 0.41	−0.04 ± 0.44	0.71 ± 0.44
		44	112	−0.14 ± 0.25	−0.03 ± 0.29	0.36 ± 0.20	−0.04 ± 0.42	−0.03 ± 0.59	0.79 ± 0.46
SulaNE	300–20	76	83	−0.21 ± 0.36	0.04 ± 0.27	−0.05 ± 0.34	0.22 ± 0.64	0.35 ± 0.65	1.07 ± 0.84
		48	97	−0.11 ± 0.29	0.04 ± 0.24	−0.06 ± 0.34	0.01 ± 0.42	0.17 ± 0.55	1.03 ± 0.64
		27	96	−0.04 ± 0.27	0.08 ± 0.21	−0.14 ± 0.27	0.04 ± 0.43	0.17 ± 0.40	0.94 ± 0.76
	150–210	76	533	0.07 ± 0.23	−0.03 ± 0.26	−0.27 ± 0.28	0.08 ± 0.37	0.22 ± 0.46	1.34 ± 0.76
		48	637	0.06 ± 0.24	−0.08 ± 0.26	−0.10 ± 0.28	0.15 ± 0.37	0.25 ± 0.43	1.55 ± 0.80
		27	637	0.07 ± 0.23	−0.14 ± 0.26	0.04 ± 0.25	0.13 ± 0.39	0.32 ± 0.43	1.52 ± 0.75
SulaSW	135–165	94	92	−0.13 ± 0.28	0.14 ± 0.22	−0.50 ± 0.23	0.44 ± 0.67	0.78 ± 0.63	0.97 ± 0.78

(*continued on next column*)

Table 7 (*continued*)

Mast	Sector (°)	H	N	γ_u	γ_v	γ_w	κ_u	κ_v	κ_w
		75	120	−0.12 ± 0.26	0.09 ± 0.18	−0.57 ± 0.25	0.44 ± 0.53	0.71 ± 0.57	1.43 ± 0.93
		50	131	−0.11 ± 0.22	0.01 ± 0.18	−0.45 ± 0.25	0.31 ± 0.37	0.38 ± 0.40	1.50 ± 0.84
		27	80	0.07 ± 0.19	0.17 ± 0.17	−0.40 ± 0.16	0.25 ± 0.29	0.21 ± 0.26	0.91 ± 0.47
	285–315	94	34	−0.20 ± 0.27	0.06 ± 0.19	−0.21 ± 0.20	0.07 ± 0.35	0.49 ± 0.37	0.70 ± 0.67
		75	48	−0.09 ± 0.28	0.13 ± 0.19	−0.23 ± 0.13	−0.02 ± 0.30	0.40 ± 0.35	0.51 ± 0.47
		50	52	−0.03 ± 0.25	0.09 ± 0.20	−0.20 ± 0.12	−0.00 ± 0.31	0.32 ± 0.35	0.41 ± 0.27
		27	31	0.01 ± 0.19	0.13 ± 0.20	−0.19 ± 0.11	−0.03 ± 0.16	0.42 ± 0.40	0.85 ± 0.27
	315–345	94	39	−0.09 ± 0.23	−0.07 ± 0.20	−0.15 ± 0.23	−0.03 ± 0.31	0.06 ± 0.36	0.70 ± 0.66
		75	37	−0.10 ± 0.19	−0.10 ± 0.22	−0.18 ± 0.22	−0.06 ± 0.31	0.22 ± 0.60	0.91 ± 0.46
		50	33	−0.10 ± 0.20	−0.09 ± 0.28	−0.12 ± 0.25	0.01 ± 0.37	0.23 ± 0.47	0.74 ± 0.36
		27	39	−0.09 ± 0.24	−0.21 ± 0.29	−0.10 ± 0.21	0.08 ± 0.36	0.37 ± 0.54	1.19 ± 0.52
SulaSE	270–330	62	128	0.01 ± 0.24	0.05 ± 0.24	−0.23 ± 0.30	0.06 ± 0.37	0.25 ± 0.42	0.92 ± 0.82
		40	121	0.01 ± 0.27	0.12 ± 0.23	−0.17 ± 0.29	0.17 ± 0.39	0.34 ± 0.39	1.22 ± 0.64
		13	59	−0.08 ± 0.22	0.21 ± 0.24	−0.24 ± 0.17	0.12 ± 0.42	0.43 ± 0.34	0.68 ± 0.44
HalsaW	150–180	50	170	−0.24 ± 0.30	0.00 ± 0.33	0.19 ± 0.23	0.25 ± 0.79	0.53 ± 0.66	1.20 ± 0.86
		31	155	−0.19 ± 0.21	0.05 ± 0.33	0.17 ± 0.23	0.05 ± 0.43	0.56 ± 0.89	1.15 ± 0.87
		12	114	−0.04 ± 0.19	0.02 ± 0.26	0.15 ± 0.19	−0.06 ± 0.61	0.39 ± 0.65	0.83 ± 0.62
	285–360	50	27	0.09 ± 0.22	−0.13 ± 0.19	−0.08 ± 0.12	−0.01 ± 0.29	0.29 ± 0.38	0.88 ± 0.64
		31	24	0.14 ± 0.22	−0.24 ± 0.24	−0.09 ± 0.18	−0.00 ± 0.35	0.29 ± 0.52	1.06 ± 0.53
		12	21	0.10 ± 0.18	−0.27 ± 0.20	−0.01 ± 0.24	0.40 ± 0.41	0.37 ± 0.43	1.76 ± 0.79
HalsaE	150–180	48	199	−0.10 ± 0.21	−0.18 ± 0.21	−0.01 ± 0.22	0.05 ± 0.31	0.32 ± 0.37	0.95 ± 0.51
		31	172	−0.29 ± 0.24	−0.40 ± 0.25	0.35 ± 0.17	0.70 ± 0.55	0.91 ± 0.55	1.86 ± 0.61
	210–285	48	33	0.19 ± 0.20	0.09 ± 0.24	−0.22 ± 0.16	−0.05 ± 0.32	0.19 ± 0.34	0.96 ± 0.41
		31	19	0.25 ± 0.20	0.10 ± 0.31	−0.20 ± 0.17	−0.00 ± 0.23	0.47 ± 0.43	1.45 ± 0.54
	300–360	48	43	0.05 ± 0.26	0.01 ± 0.26	0.08 ± 0.25	−0.15 ± 0.28	0.12 ± 0.46	0.91 ± 0.51
		31	31	0.11 ± 0.24	−0.02 ± 0.24	0.06 ± 0.25	−0.02 ± 0.36	0.21 ± 0.56	1.12 ± 0.56
JulW	120–195	68	96	−0.21 ± 0.30	0.28 ± 0.30	0.15 ± 0.36	0.29 ± 0.62	0.36 ± 0.72	1.31 ± 1.11
		52	192	−0.17 ± 0.28	0.22 ± 0.25	0.10 ± 0.35	0.14 ± 0.44	0.23 ± 0.56	1.29 ± 0.96
		32	198	−0.14 ± 0.30	0.20 ± 0.23	0.07 ± 0.36	0.13 ± 0.42	0.22 ± 0.61	1.20 ± 0.90
	330–360	68	45	−0.26 ± 0.22	−0.23 ± 0.22	−0.17 ± 0.27	0.32 ± 0.56	0.62 ± 0.57	0.84 ± 0.79
		52	92	−0.27 ± 0.21	−0.25 ± 0.22	−0.20 ± 0.26	0.34 ± 0.52	0.60 ± 0.42	0.91 ± 0.76
		32	74	−0.25 ± 0.18	−0.29 ± 0.19	−0.19 ± 0.23	0.38 ± 0.36	0.52 ± 0.31	0.95 ± 0.46
JulE	120–195	50	97	0.02 ± 0.28	−0.10 ± 0.29	−0.05 ± 0.21	0.02 ± 0.35	0.32 ± 0.44	0.91 ± 0.73
		31	102	0.04 ± 0.24	−0.08 ± 0.33	−0.02 ± 0.20	0.00 ± 0.29	0.32 ± 0.59	1.08 ± 0.69
		12	5	−0.55 ± 0.27	0.33 ± 0.36	−0.08 ± 0.07	1.09 ± 0.78	1.32 ± 0.37	0.74 ± 0.26
	210–285	50	111	0.08 ± 0.18	0.02 ± 0.19	−0.29 ± 0.13	−0.08 ± 0.28	0.22 ± 0.33	0.67 ± 0.36
		31	110	0.13 ± 0.19	0.04 ± 0.19	−0.35 ± 0.13	−0.05 ± 0.32	0.17 ± 0.31	0.98 ± 0.42
		12	49	0.11 ± 0.26	−0.02 ± 0.16	−0.15 ± 0.25	0.19 ± 0.40	0.20 ± 0.33	1.54 ± 0.54
	300–360	50	91	−0.06 ± 0.30	−0.04 ± 0.31	0.20 ± 0.19	−0.07 ± 0.41	0.06 ± 0.61	0.69 ± 0.39
		31	91	−0.04 ± 0.24	−0.05 ± 0.29	0.17 ± 0.18	−0.12 ± 0.33	0.05 ± 0.43	0.78 ± 0.41
		12	75	0.04 ± 0.21	−0.02 ± 0.26	0.29 ± 0.12	−0.13 ± 0.30	0.10 ± 0.43	0.72 ± 0.35

Table 8
Turbulence intensity: Wind direction, height above terrain (H), number of samples (N) and the turbulence intensities (*TI*) and associated standard deviations at the met-masts at Sulafjorden, Halsafjorden and Julsundet with $u \geq 12$ m s^{-1} at every height. Data outside the 1st and 99th percentile were considered as outliers and removed.

Mast	Sector (°)	Sensor height (H)	N	I_u	I_v	I_w
SulaNW	135–165	92	64	0.12 ± 0.03	0.11 ± 0.03	0.11 ± 0.02
		71	100	0.13 ± 0.03	0.12 ± 0.02	0.12 ± 0.03
		44	69	0.13 ± 0.02	0.11 ± 0.02	0.10 ± 0.02
	165–185	92	537	0.16 ± 0.03	0.12 ± 0.02	0.16 ± 0.03
		71	522	0.16 ± 0.03	0.13 ± 0.02	0.16 ± 0.03
		44	519	0.17 ± 0.03	0.13 ± 0.02	0.14 ± 0.02
	300–330	92	96	0.07 ± 0.02	0.08 ± 0.03	0.06 ± 0.01
		71	87	0.08 ± 0.02	0.09 ± 0.03	0.06 ± 0.01
		44	112	0.08 ± 0.02	0.09 ± 0.03	0.05 ± 0.01
SulaNE	300–20	76	83	0.12 ± 0.04	0.12 ± 0.04	0.10 ± 0.03
		48	97	0.13 ± 0.03	0.13 ± 0.04	0.09 ± 0.03
		27	96	0.13 ± 0.04	0.13 ± 0.04	0.09 ± 0.02
	150–210	76	533	0.10 ± 0.02	0.11 ± 0.03	0.08 ± 0.02
		48	637	0.10 ± 0.02	0.11 ± 0.03	0.07 ± 0.02
		27	637	0.11 ± 0.02	0.11 ± 0.03	0.07 ± 0.01
SulaSW	135–165	94	92	0.20 ± 0.05	0.16 ± 0.03	0.19 ± 0.04
		75	120	0.20 ± 0.04	0.16 ± 0.03	0.19 ± 0.04
		50	131	0.22 ± 0.03	0.17 ± 0.03	0.20 ± 0.04
		27	80	0.24 ± 0.03	0.20 ± 0.02	0.22 ± 0.03
	285–315	94	34	0.16 ± 0.03	0.13 ± 0.03	0.14 ± 0.02
		75	48	0.17 ± 0.03	0.14 ± 0.04	0.15 ± 0.03
		50	52	0.18 ± 0.03	0.14 ± 0.04	0.15 ± 0.02
		27	31	0.21 ± 0.02	0.17 ± 0.03	0.14 ± 0.01
	315–345	94	39	0.15 ± 0.04	0.15 ± 0.04	0.12 ± 0.04
		75	37	0.13 ± 0.04	0.13 ± 0.04	0.09 ± 0.03
		50	33	0.13 ± 0.03	0.13 ± 0.03	0.09 ± 0.02
		27	39	0.15 ± 0.05	0.15 ± 0.04	0.09 ± 0.04

(*continued on next column*)

Table 8 (*continued*)

Mast	Sector (°)	Sensor height (H)	N	I_u	I_v	I_w
SulaSE	270–330	62	128	0.14 ± 0.04	0.12 ± 0.03	0.11 ± 0.04
		40	121	0.14 ± 0.04	0.12 ± 0.03	0.10 ± 0.03
		13	59	0.19 ± 0.04	0.15 ± 0.02	0.13 ± 0.02
HalsaW	150–180	50	170	0.10 ± 0.02	0.09 ± 0.02	0.05 ± 0.01
		31	155	0.11 ± 0.02	0.09 ± 0.02	0.05 ± 0.01
		12	114	0.11 ± 0.01	0.10 ± 0.01	0.06 ± 0.01
	285–360	50	27	0.18 ± 0.05	0.16 ± 0.04	0.11 ± 0.04
		31	24	0.18 ± 0.05	0.17 ± 0.05	0.09 ± 0.04
		12	21	0.17 ± 0.03	0.15 ± 0.03	0.07 ± 0.02
HalsaE	150–180	48	199	0.11 ± 0.03	0.10 ± 0.02	0.06 ± 0.01
		31	172	0.14 ± 0.04	0.12 ± 0.02	0.07 ± 0.02
	210–285	48	33	0.17 ± 0.02	0.15 ± 0.03	0.10 ± 0.01
		31	19	0.16 ± 0.03	0.16 ± 0.03	0.08 ± 0.02
	300–360	48	43	0.14 ± 0.03	0.14 ± 0.03	0.08 ± 0.02
		31	31	0.15 ± 0.03	0.15 ± 0.04	0.08 ± 0.02
JulW	120–195	68	96	0.09 ± 0.04	0.09 ± 0.04	0.05 ± 0.03
		52	192	0.09 ± 0.04	0.10 ± 0.04	0.05 ± 0.03
		32	198	0.10 ± 0.03	0.11 ± 0.04	0.05 ± 0.02
	330–360	68	45	0.15 ± 0.04	0.12 ± 0.03	0.10 ± 0.04
		52	92	0.15 ± 0.04	0.12 ± 0.03	0.10 ± 0.04
		32	74	0.16 ± 0.04	0.13 ± 0.03	0.09 ± 0.03
JulE	120–195	50	97	0.11 ± 0.02	0.11 ± 0.03	0.07 ± 0.02
		31	102	0.11 ± 0.02	0.11 ± 0.03	0.07 ± 0.02
		12	5	0.13 ± 0.01	0.10 ± 0.01	0.07 ± 0.01
	210–285	50	111	0.18 ± 0.03	0.16 ± 0.03	0.12 ± 0.02
		31	110	0.18 ± 0.03	0.16 ± 0.03	0.10 ± 0.01
		12	49	0.22 ± 0.04	0.20 ± 0.02	0.09 ± 0.01
	300–360	50	91	0.10 ± 0.02	0.10 ± 0.03	0.05 ± 0.01
		31	91	0.10 ± 0.02	0.10 ± 0.03	0.05 ± 0.01
		12	75	0.11 ± 0.01	0.12 ± 0.03	0.05 ± 0.00

Table 9

Normalized standard deviation: Wind direction, height above terrain (H), number of samples (N), normalized standard deviation and associated standard deviation at the met-masts at Sulafjorden, Halsafjorden and Julsundet. Wind velocity above 12 m s^{-1} for all elevations. Data outside the 1st and 99th percentile were considered as outliers and removed.

Mast	Sector (°)	Sensor height (H)	N	σ_w/u_*	σ_v/u_*	σ_u/u_*	σ_w/σ_u	σ_v/σ_u
SulaNW	135–165	92	64	2.05 ± 0.30	2.04 ± 0.31	2.22 ± 0.34	0.93 ± 0.11	0.93 ± 0.13
		71	100	2.07 ± 0.34	2.04 ± 0.46	2.32 ± 0.46	0.90 ± 0.12	0.88 ± 0.12
		44	69	1.97 ± 0.34	2.37 ± 0.42	2.62 ± 0.51	0.76 ± 0.09	0.92 ± 0.14
	165–185	92	537	2.13 ± 0.31	1.64 ± 0.28	2.14 ± 0.32	1.00 ± 0.08	0.77 ± 0.08
		71	522	2.04 ± 0.33	1.63 ± 0.31	2.11 ± 0.35	0.97 ± 0.07	0.77 ± 0.08
		44	519	1.98 ± 0.33	1.83 ± 0.35	2.32 ± 0.42	0.85 ± 0.07	0.79 ± 0.07
	300–330	92	96	1.61 ± 0.29	2.37 ± 0.60	2.08 ± 0.46	0.79 ± 0.15	1.16 ± 0.26
		71	87	1.49 ± 0.24	2.33 ± 0.54	1.99 ± 0.42	0.77 ± 0.13	1.18 ± 0.23
		44	112	1.41 ± 0.19	2.39 ± 0.56	2.09 ± 0.38	0.68 ± 0.10	1.15 ± 0.24
SulaNE	300–20	76	83	1.77 ± 0.30	2.23 ± 0.62	2.28 ± 0.50	0.79 ± 0.10	0.98 ± 0.18
		48	97	1.71 ± 0.33	2.35 ± 0.71	2.40 ± 0.52	0.72 ± 0.10	0.97 ± 0.17
		27	96	1.57 ± 0.24	2.22 ± 0.64	2.26 ± 0.52	0.71 ± 0.11	0.98 ± 0.18
	150–210	76	533	1.80 ± 0.27	2.62 ± 0.45	2.45 ± 0.41	0.74 ± 0.10	1.08 ± 0.17
		48	637	1.76 ± 0.30	2.81 ± 0.56	2.65 ± 0.51	0.67 ± 0.09	1.07 ± 0.17
		27	637	1.53 ± 0.27	2.68 ± 0.56	2.57 ± 0.57	0.61 ± 0.08	1.06 ± 0.16
SulaSW	135–165	94	92	1.73 ± 0.23	1.48 ± 0.34	1.82 ± 0.31	0.96 ± 0.08	0.81 ± 0.11
		75	120	1.78 ± 0.21	1.50 ± 0.26	1.89 ± 0.24	0.95 ± 0.10	0.79 ± 0.10
		50	131	1.68 ± 0.24	1.44 ± 0.12	1.81 ± 0.17	0.93 ± 0.12	0.80 ± 0.09
		27	80	1.58 ± 0.21	1.44 ± 0.10	1.74 ± 0.18	0.91 ± 0.07	0.83 ± 0.08
	285–315	94	34	1.97 ± 0.26	1.78 ± 0.31	2.27 ± 0.26	0.87 ± 0.08	0.78 ± 0.11
		75	48	1.92 ± 0.29	1.76 ± 0.33	2.21 ± 0.30	0.87 ± 0.08	0.80 ± 0.12
		50	52	1.77 ± 0.24	1.72 ± 0.33	2.19 ± 0.27	0.81 ± 0.07	0.79 ± 0.15
		27	31	1.59 ± 0.15	1.96 ± 0.30	2.33 ± 0.23	0.68 ± 0.05	0.84 ± 0.14
	315–345	94	39	1.86 ± 0.26	2.40 ± 0.49	2.37 ± 0.39	0.80 ± 0.12	1.02 ± 0.12
		75	37	1.73 ± 0.29	2.47 ± 0.48	2.42 ± 0.44	0.72 ± 0.09	1.03 ± 0.12
		50	33	1.46 ± 0.27	2.28 ± 0.42	2.24 ± 0.39	0.65 ± 0.07	1.02 ± 0.11
		27	39	1.39 ± 0.22	2.38 ± 0.34	2.38 ± 0.39	0.59 ± 0.08	1.01 ± 0.12
SulaSE	270–330	62	130	1.58 ± 0.25	1.89 ± 0.51	2.10 ± 0.39	0.77 ± 0.12	0.91 ± 0.19
		40	121	1.47 ± 0.23	1.96 ± 0.42	2.16 ± 0.38	0.69 ± 0.09	0.92 ± 0.18
		13	59	1.34 ± 0.13	1.53 ± 0.16	1.93 ± 0.24	0.70 ± 0.04	0.81 ± 0.13
HalsaW	150–180	50	170	1.42 ± 0.20	2.32 ± 0.42	2.64 ± 0.43	0.54 ± 0.06	0.88 ± 0.12
		31	155	1.35 ± 0.19	2.34 ± 0.38	2.63 ± 0.43	0.52 ± 0.05	0.89 ± 0.10
		12	114	1.19 ± 0.08	2.06 ± 0.24	2.29 ± 0.21	0.52 ± 0.04	0.90 ± 0.09
	285–360	50	27	1.52 ± 0.26	2.43 ± 0.70	2.74 ± 0.74	0.57 ± 0.08	0.89 ± 0.12
		31	24	1.52 ± 0.21	2.87 ± 0.73	3.08 ± 0.71	0.51 ± 0.09	0.93 ± 0.11
		12	21	1.42 ± 0.23	3.21 ± 0.54	3.59 ± 0.86	0.40 ± 0.05	0.91 ± 0.13
HalsaE	150–180	48	199	1.57 ± 0.29	2.61 ± 0.52	2.91 ± 0.62	0.55 ± 0.05	0.91 ± 0.11

(*continued on next column*)

Table 9 (*continued*)

Mast	Sector (°)	Sensor height (H)	N	σ_w/u_*	σ_v/u_*	σ_u/u_*	σ_w/σ_u	σ_v/σ_u
		31	172	1.58 ± 0.27	2.52 ± 0.49	3.03 ± 0.61	0.52 ± 0.04	0.84 ± 0.10
	210–285	48	33	1.52 ± 0.17	2.41 ± 0.31	2.61 ± 0.27	0.59 ± 0.05	0.93 ± 0.10
		31	19	1.47 ± 0.24	2.86 ± 0.43	2.81 ± 0.40	0.52 ± 0.05	1.02 ± 0.11
	300–360	48	43	1.39 ± 0.27	2.45 ± 0.48	2.55 ± 0.58	0.56 ± 0.08	0.98 ± 0.16
		31	31	1.42 ± 0.33	2.78 ± 0.57	2.89 ± 0.83	0.50 ± 0.06	0.99 ± 0.18
JulW	120–195	68	96	1.49 ± 0.28	2.71 ± 0.56	2.66 ± 0.66	0.58 ± 0.11	1.05 ± 0.19
		52	192	1.46 ± 0.29	2.76 ± 0.53	2.62 ± 0.65	0.57 ± 0.10	1.08 ± 0.20
		32	198	1.38 ± 0.28	2.85 ± 0.52	2.61 ± 0.56	0.53 ± 0.09	1.12 ± 0.23
	330–360	68	45	1.58 ± 0.29	1.97 ± 0.40	2.45 ± 0.36	0.65 ± 0.09	0.81 ± 0.11
		52	92	1.58 ± 0.23	2.04 ± 0.48	2.51 ± 0.35	0.63 ± 0.08	0.81 ± 0.12
		32	74	1.53 ± 0.13	2.13 ± 0.31	2.61 ± 0.25	0.59 ± 0.05	0.82 ± 0.12
JulE	120–195	50	97	1.65 ± 0.27	2.65 ± 0.68	2.74 ± 0.55	0.61 ± 0.11	0.97 ± 0.17
		31	102	1.61 ± 0.29	2.85 ± 0.69	2.81 ± 0.48	0.58 ± 0.11	1.02 ± 0.21
		12	5	1.83 ± 0.28	2.42 ± 0.49	3.35 ± 0.48	0.55 ± 0.03	0.72 ± 0.05
	210–285	50	111	1.80 ± 0.32	2.44 ± 0.47	2.84 ± 0.49	0.64 ± 0.05	0.86 ± 0.09
		31	110	1.86 ± 0.31	2.97 ± 0.53	3.31 ± 0.53	0.56 ± 0.04	0.90 ± 0.10
		12	49	1.62 ± 0.42	3.78 ± 1.23	4.12 ± 1.05	0.39 ± 0.02	0.90 ± 0.12
	300–360	50	91	1.21 ± 0.13	2.32 ± 0.59	2.25 ± 0.40	0.55 ± 0.08	1.04 ± 0.22
		31	91	1.20 ± 0.14	2.39 ± 0.66	2.32 ± 0.40	0.53 ± 0.07	1.03 ± 0.21
		12	75	1.05 ± 0.08	2.30 ± 0.56	2.27 ± 0.37	0.47 ± 0.05	1.01 ± 0.19

Table 10
Normalized momentum fluxes: Wind direction, height above terrain (H), number of samples (N), horizontal and vertical momentum fluxes and associated standard deviation at the met-masts at Sulafjorden, Halsafjorden and Julsundet. Wind velocity above 12 m s^{-1} for all elevations. Data outside the 1st and 99th percentile were considered as outliers and removed.

Mast	Sector (°)	Sensor height (H)	N	$\frac{\overline{u'v'}}{u_*^2}$	$\frac{\overline{u'w'}}{u_*^2}$	$\frac{\overline{v'w'}}{u_*^2}$
SulaNW	135–165	92	64	0.44 ± 0.74	−0.68 ± 0.36	−0.56 ± 0.32
		71	100	0.32 ± 0.90	−0.58 ± 0.39	−0.67 ± 0.27
		44	69	0.23 ± 1.13	−0.55 ± 0.33	−0.74 ± 0.20
	165–185	92	537	0.56 ± 0.60	−0.73 ± 0.23	−0.45 ± 0.46
		71	522	0.68 ± 0.62	−0.72 ± 0.21	−0.55 ± 0.36
		44	519	1.00 ± 0.79	−0.69 ± 0.20	−0.64 ± 0.27
	300–330	92	96	0.26 ± 1.55	−0.87 ± 0.22	0.11 ± 0.42
		71	87	0.20 ± 1.35	−0.91 ± 0.19	0.11 ± 0.36
		44	112	0.23 ± 1.12	−0.92 ± 0.16	0.13 ± 0.34
SulaNE	300–20	76	83	−0.14 ± 1.13	−0.62 ± 0.37	−0.60 ± 0.35
		48	97	−0.33 ± 1.24	−0.72 ± 0.36	−0.41 ± 0.43
		27	96	−0.55 ± 1.11	−0.64 ± 0.32	−0.59 ± 0.38
	150–210	76	533	0.24 ± 1.31	−0.80 ± 0.30	0.09 ± 0.52
		48	637	0.36 ± 1.48	−0.79 ± 0.27	0.25 ± 0.50
		27	637	0.86 ± 1.54	−0.76 ± 0.24	0.47 ± 0.37
SulaSW	135–165	94	92	0.48 ± 0.45	−0.57 ± 0.26	−0.76 ± 0.19
		75	120	0.39 ± 0.41	−0.48 ± 0.27	−0.82 ± 0.16
		50	131	0.30 ± 0.26	−0.47 ± 0.27	−0.83 ± 0.13
		27	80	0.14 ± 0.23	−0.43 ± 0.25	−0.86 ± 0.10
	285–315	94	34	−0.39 ± 0.39	−0.84 ± 0.28	0.25 ± 0.40
		75	48	−0.33 ± 0.44	−0.90 ± 0.18	0.22 ± 0.34
		50	52	−0.23 ± 0.42	−0.88 ± 0.14	0.37 ± 0.26
		27	31	−0.26 ± 0.36	−0.78 ± 0.15	0.58 ± 0.19
	315–345	94	39	0.55 ± 0.92	−0.84 ± 0.24	0.32 ± 0.37
		75	37	0.79 ± 1.24	−0.72 ± 0.36	0.43 ± 0.42
		50	33	0.73 ± 0.98	−0.68 ± 0.28	0.61 ± 0.30
		27	39	0.72 ± 0.95	−0.53 ± 0.28	0.77 ± 0.24
SulaSE	270–330	62	128	0.06 ± 0.83	−0.55 ± 0.41	−0.66 ± 0.30
		40	121	0.13 ± 0.77	−0.55 ± 0.35	−0.74 ± 0.19
		13	59	−0.41 ± 0.46	−0.63 ± 0.24	−0.70 ± 0.23
HalsaW	150–180	50	170	−0.87 ± 1.08	−0.91 ± 0.18	−0.20 ± 0.31
		31	155	−0.78 ± 1.03	−0.92 ± 0.15	−0.21 ± 0.29
		12	114	−0.35 ± 0.51	−0.93 ± 0.14	−0.25 ± 0.24
	285–360	50	27	0.46 ± 1.13	−0.93 ± 0.17	0.11 ± 0.31
		31	24	0.32 ± 2.25	−0.96 ± 0.07	0.16 ± 0.24
		12	21	0.29 ± 2.62	−0.90 ± 0.09	0.28 ± 0.34
HalsaE	150–180	48	199	0.68 ± 1.16	−0.89 ± 0.18	−0.02 ± 0.41
		31	172	0.98 ± 1.18	−0.92 ± 0.15	−0.08 ± 0.36
	210–285	48	33	0.15 ± 0.84	−0.96 ± 0.07	0.15 ± 0.24
		31	19	−0.13 ± 1.10	−0.87 ± 0.12	0.33 ± 0.34
	300–360	48	43	−0.20 ± 1.50	−0.86 ± 0.27	−0.20 ± 0.39
		31	31	−0.67 ± 2.10	−0.84 ± 0.35	−0.18 ± 0.39
JulW	120–195	68	96	−1.72 ± 1.71	−0.35 ± 0.53	−0.61 ± 0.49
		52	192	−1.77 ± 1.50	−0.46 ± 0.43	−0.63 ± 0.46
		32	198	−1.90 ± 1.49	−0.48 ± 0.39	−0.65 ± 0.43
	330–360	68	45	0.52 ± 0.73	−0.76 ± 0.28	0.53 ± 0.26

(*continued on next column*)

Table 10 (*continued*)

Mast	Sector (°)	Sensor height (H)	N	$\frac{u'v'}{u_*^2}$	$\frac{u'w'}{u_*^2}$	$\frac{v'w'}{u_*^2}$
		52	92	0.58 ± 0.60	−0.74 ± 0.26	0.56 ± 0.27
		32	74	0.77 ± 0.54	−0.65 ± 0.20	0.69 ± 0.25
JulE	120–195	50	97	0.51 ± 1.67	−0.86 ± 0.18	−0.27 ± 0.41
		31	102	0.38 ± 1.63	−0.81 ± 0.18	−0.41 ± 0.37
		12	5	−0.83 ± 0.53	−0.67 ± 0.49	−0.54 ± 0.41
	210–285	50	111	0.10 ± 1.08	−0.74 ± 0.38	0.26 ± 0.49
		31	110	0.14 ± 1.76	−0.76 ± 0.37	0.01 ± 0.54
		12	49	0.83 ± 2.86	−0.66 ± 0.32	0.62 ± 0.28
	300–360	50	91	0.18 ± 1.63	−0.93 ± 0.15	−0.16 ± 0.28
		31	91	0.01 ± 1.91	−0.98 ± 0.04	0.03 ± 0.20
		12	75	−0.00 ± 1.56	−0.96 ± 0.07	0.18 ± 0.19

References

Ágústsson, H., Broe, B.R., Hoem, M.E., 2020. Analysis of Wind Measurements from 6 Masts at Sulafjorden 24.11.2016-31.03.2020. Technical Report KVT/HA/2020/R046 Kjeller Vindteknikk, Norconsult.

Ágústsson, H., Ólafsson, H., 2004. Mean gust factors in complex terrain. Meteorol. Z. 13, 149–155. https://doi.org/10.1127/0941-2948/2004/0013-0149.

Argentini, T., Rocchi, D., Somaschini, C., 2020. Effect of the low-frequency turbulence on the aeroelastic response of a long-span bridge in wind tunnel. J. Wind Eng. Ind. Aerod. 197, 104072. https://doi.org/10.1016/j.jweia.2019.104072.

Barthelmie, R., 1999. The effects of atmospheric stability on coastal wind climates. Meteorol. Appl.: J. Forecast. Pract. Appl. Tech. Model. 6, 39–47. https://doi.org/10.1017/s1350482799000961.

Bietry, J., Delaunay, D., Conti, E., 1995. Comparison of full-scale measurement and computation of wind effects on a cable-stayed bridge. J. Wind Eng. Ind. Aerod. 57, 225–235. https://doi.org/10.1016/0167-6105(94)00110-Y.

Billesbach, D.P., Chan, S.W., Cook, D.R., Papale, D., Bracho-Garrillo, R., Verfallie, J., Vargas, R., Biraud, S.C., 2019. Effects of the Gill-Solent WindMaster-Pro "w–boost" firmware bug on eddy covariance fluxes and some simple recovery strategies. Agric. For. Meteorol. 265, 145–151. https://doi.org/10.1016/j.agrformet.2018.11.010.

Bowen, A.J., Flay, R.G., Panofsky, H.A., 1983. Vertical coherence and phase delay between wind components in strong winds below 20 m. Boundary-Layer Meteorol. 26, 313–324. https://doi.org/10.1007/BF00119530.

Cao, S., 2013. Strong winds and their characteristics. In: Tamura, Y., Kareem, A. (Eds.), Advanced Structural Wind Engineering. Springer, Tokyo, pp. 1–25. https://doi.org/10.1007/978-4-431-54337-4_1.

Cheynet, E., 2019. Influence of the measurement height on the vertical coherence of natural wind. In: Ricciardelli, F., Avossa, A. (Eds.), Proceedings of the XV Conference of the Italian Association for Wind Engineering. IN VENTO 2018. Lecture Notes in Civil Engineering, vol. 27, pp. 207–221. https://doi.org/10.1007/978-3-030-12815-9_17.

Cheynet, E., Jakobsen, J., Snæbjörnsson, J., Ágústsson, H., Harstveit, K., 2018a. Complementary use of wind lidars and land-based met-masts for wind measurements in a wide fjord. JPhCS 1104, 012028. https://doi.org/10.1088/1742-6596/1104/1/012028.

Cheynet, E., Jakobsen, J.B., Obhrai, C., 2017a. Spectral characteristics of surface-layer turbulence in the north sea. Energy Procedia 137, 414–427. https://doi.org/10.1016/j.egypro.2017.10.366.

Cheynet, E., Jakobsen, J.B., Reuder, J., 2018b. Velocity spectra and coherence estimates in the marine atmospheric boundary layer. Boundary-Layer Meteorol. 169, 429–460. https://doi.org/10.1007/s10546-018-0382-2.

Cheynet, E., Jakobsen, J.B., Snæbjörnsson, J., 2016. Buffeting response of a suspension bridge in complex terrain. Eng. Struct. 128, 474–487. https://doi.org/10.1016/J.ENGSTRUCT.2016.09.060.

Cheynet, E., Jakobsen, J.B., Snæbjörnsson, J., 2019. Flow distortion recorded by sonic anemometers on a long-span bridge: towards a better modelling of the dynamic wind load in full-scale. J. Sound Vib. 450, 214–230. https://doi.org/10.1016/j.jsv.2019.03.013.

Cheynet, E., Jakobsen, J.B., Snæbjörnsson, J., Angelou, N., Mikkelsen, T., Sjöholm, M., Svardal, B., 2017b. Full-scale observation of the flow downstream of a suspension bridge deck. J. Wind Eng. Ind. Aerod. 171, 261–272. https://doi.org/10.1016/j.jweia.2017.10.007.

Davenport, A., 1961a. The application of statistical concepts to the wind loading of structures. Proc. Inst. Civ. Eng. 19, 449–472. https://doi.org/10.1680/iicep.1961.11304.

Davenport, A.G., 1961b. The spectrum of horizontal gustiness near the ground in high winds. Q. J. R. Meteorol. Soc. 87, 194–211. https://doi.org/10.1002/qj.49708737208.

Delaunay, D., Grillaud, G., 1998. Field measurements of the wind-induced response of a cable stayed bridge: validation of previsional studies. J. Wind Eng. Ind. Aerod. 74–76, 883–890. https://doi.org/10.1016/S0167-6105(98)00080-4.

Diana, G., Omarini, S., 2020. A non-linear method to compute the buffeting response of a bridge validation of the model through wind tunnel tests. J. Wind Eng. Ind. Aerod. 201, 104163. https://doi.org/10.1016/j.jweia.2020.104163.

Diana, G., Rocchi, D., Argentini, T., Muggiasca, S., 2010. Aerodynamic instability of a bridge deck section model: linear and nonlinear approach to force modeling. J. Wind Eng. Ind. Aerod. 98, 363–374. https://doi.org/10.1016/j.jweia.2010.01.003.

EN 1991-1-4, 2005. Eurocode 1. Actions on Structures–Part 1-4: General Actions – Wind Actions. Technical Report [Authority: The European Union Per Regulation 305/2011, Directive 98/34/EC, Directive 2004/18/EC].

Eriksen, O.K., 2020. E39, Brukrysninger Julsundet Og Halsafjorden, Møre Og Romsdal - Statusrapport for Vindmålinger Pr Desember 2019. Technical Report KVT/OKE/2020/R012 Kjeller Vindteknikk, Norconsult.

Fenerci, A., Øiseth, O., 2017. Measured buffeting response of a long-span suspension bridge compared with numerical predictions based on design wind spectra. J. Struct. Eng. 143, 04017131 https://doi.org/10.1061/(ASCE)ST.1943-541X.0001873.

Fenerci, A., Øiseth, O., 2018a. Site-specific data-driven probabilistic wind field modeling for the wind-induced response prediction of cable-supported bridges. J. Wind Eng. Ind. Aerod. 181, 161–179. https://doi.org/10.1016/j.jweia.2018.09.002.

Fenerci, A., Øiseth, O., 2018b. Strong wind characteristics and dynamic response of a long-span suspension bridge during a storm. J. Wind Eng. Ind. Aerod. 172, 116–138. https://doi.org/10.1016/j.jweia.2017.10.030.

Fenerci, A., Øiseth, O., Rønnquist, A., 2017. Long-term monitoring of wind field characteristics and dynamic response of a long-span suspension bridge in complex terrain. Eng. Struct. 147, 269–284. https://doi.org/10.1016/j.engstruct.2017.05.070.

Fernández-Cabán, P., Masters, F., 2017. Near surface wind longitudinal velocity positively skews with increasing aerodynamic roughness length. J. Wind Eng. Ind. Aerod. 169, 94–105. https://doi.org/10.1016/j.jweia.2017.06.007.

de Franceschi, M., Zardi, D., Tagliazucca, M., Tampieri, F., 2009. Analysis of second-order moments in surface layer turbulence in an Alpine valley. Q. J. R. Meteorol. Soc. 135, 1750–1765. https://doi.org/10.1002/qj.506.

Frank, H.P., 1996. A simple spectral model for the modification of turbulence in flow over gentle hills. Boundary-Layer Meteorol. 79, 345–373. https://doi.org/10.1007/BF00119404.

Frost, R., 1948. Atmospheric turbulence. Q. J. R. Meteorol. Soc. 74, 316–338. https://doi.org/10.1002/qj.49707432106.

Furevik, B., Ágústsson, H., Borg, A.L., Nyhammer, F., 2019. The E39 Coastal Highway Observational Dataset – Atmospheric Flow in Complex Coastal Terrain in Mid-Norway. Technical Report Norwegian Meteorological Institute. https://doi.org/10.21343/z9n1-qw63.

Furevik, B.R., Ágústson, H., Lauen Borg, A., Zakari, M., Nyhammer, F., Gausen, M., 2020. Meteorological observations in tall masts for mapping of atmospheric flow in Norwegian fjords. Earth Syst. Sci. Data Discuss. 1–28. https://doi.org/10.5194/essd-2020-32.

Geernaert, G.L., 1988. Measurements of the angle between the wind vector and wind stress vector in the surface layer over the North Sea. J. Geophys. Res. 93, 8215. https://doi.org/10.1029/jc093ic07p08215.

Gill Instruments, 2016. Technical Key Note KN1509v3*. URL: http://gillinstruments.com/data/manuals/KN1509.pdf.

Golzio, A., Bollati, I.M., Ferrarese, S., 2019. An assessment of coordinate rotation methods in sonic anemometer measurements of turbulent fluxes over complex mountainous terrain. Atmosphere 10, 324. https://doi.org/10.3390/atmos10060324.

Grønås, S., Sandvik, A.D., 1999. Numerical simulations of local winds over steep orography in the storm over north Norway on October 12, 1996. J. Geophys. Res.: Atmosphere 104, 9107–9120. https://doi.org/10.1029/1998JD200115.

Guarino, M.-V., Teixeira, M.A.C., Ambaum, M.H.P., 2016. Turbulence generation by mountain wave breaking in flows with directional wind shear. Q. J. R. Meteorol. Soc. 142, 2715–2726. https://doi.org/10.1002/qj.2862.

Gurley, K., Kareem, A., 1997. Analysis interpretation modeling and simulation of unsteady wind and pressure data. J. Wind Eng. Ind. Aerod. 69–71, 657–669. https://doi.org/10.1016/S0167-6105(97)00195-5.

Harstveit, K., 1996. Full scale measurements of gust factors and turbulence intensity, and their relations in hilly terrain. J. Wind Eng. Ind. Aerod. 61, 195–205. https://doi.org/10.1016/0167-6105(96)00047-5.

Högström, U., Hunt, J.C., Smedman, A.S., 2002. Theory and measurements for turbulence spectra and variances in the atmospheric neutral surface layer. Boundary-Layer Meteorol. 103, 101–124. https://doi.org/10.1023/A:1014579828712.

Hsu, S., Meindl, E.A., Gilhousen, D.B., 1994. Determining the power-law wind-profile exponent under near-neutral stability conditions at sea. J. Appl. Meteorol. 33, 757–765. https://doi.org/10.1175/1520-0450(1994)033¡0757:DTPLWP¿2.0.CO;2.

Hui, M., Larsen, A., Xiang, H., 2009a. Wind turbulence characteristics study at the Stonecutters bridge site: Part –I mean wind and turbulence intensities. J. Wind Eng. Ind. Aerod. 97, 22–36. https://doi.org/10.1016/J.JWEIA.2008.11.002.

Hui, M., Larsen, A., Xiang, H., 2009b. Wind turbulence characteristics study at the Stonecutters bridge site: Part – II wind power spectra, integral length scales and coherences. J. Wind Eng. Ind. Aerod. 97, 48–59. https://doi.org/10.1016/J.JWEIA.2008.11.003.

Hunt, J.C., Carlotti, P., 2001. Statistical structure at the wall of the high Reynolds number turbulent boundary layer. Flow, Turbul. Combust. 66, 453–475. https://doi.org/10.1023/A:1013519021030.

Hunt, J.C., Morrison, J.F., 2000. Eddy structure in turbulent boundary layers. Eur. J. Mech. B Fluid 19, 673–694. https://doi.org/10.1016/S0997-7546(00)00129-1.

Irwin, J.S., 1979. A theoretical variation of the wind profile power-law exponent as a function of surface roughness and stability. Atmos. Environ. 13, 191–194. https://doi.org/10.1016/0004-6981(79)90260-9, 1967.

Ishihara, T., Hibi, K., Oikawa, S., 1999. A wind tunnel study of turbulent flow over a three-dimensional steep hill. J. Wind Eng. Ind. Aerod. 83, 95–107. https://doi.org/10.1016/S0167-6105(99)00064-1.

Jackson, P.L., Steyn, D.G., 1994. Gap winds in a fjord. Part I: observations and numerical simulation. Mon. Weather Rev. 122, 2645–2665. https://doi.org/10.1175/1520-0493(1994)122¡2645:GWIAFP¿2.0.CO;2.

Jackson, P.S., Hunt, J.C.R., 1975. Turbulent wind flow over a low hill. Q. J. R. Meteorol. Soc. 101, 929–955. https://doi.org/10.1002/qj.49710143015.

Jensen, N., Hjort-Hansen, E., 1977. *Dynamic Excitation of Structures by Wind–Turbulence and Response Measurements at the Sotra Bridge*. Technical Report SINTEF Report No. STF71 A78003 Trondheim-NTH. Norway.

Kaimal, J.C., Finnigan, J.J., 1994. Atmospheric Boundary Layer Flows: Their Structure and Measurement. Oxford University Press.

Kaimal, J.C., Wyngaard, J.C., Izumi, Y., Coté, O.R., 1972. Spectral characteristics of surface-layer turbulence. Q. J. R. Meteorol. Soc. 98, 563–589. https://doi.org/10.1002/qj.49709841707.

Kareem, A.a., Tognarelli, M., Gurley, K., 1998. Modeling and analysis of quadratic term in the wind effects on structures. J. Wind Eng. Ind. Aerod. 74, 1101–1110. https://doi.org/10.1016/S0167-6105(98)00101-9.

Karmakar, D., Ray-Chaudhuri, S., Shinozuka, M., 2012. Conditional simulation of non-Gaussian wind velocity profiles: application to buffeting response of Vincent Thomas suspension bridge. Probabilist. Eng. Mech. 29, 167–175. https://doi.org/10.1016/j.probengmech.2011.11.005.

Klipp, C., 2018. Turbulent friction velocity calculated from the Reynolds stress Tensor. J. Atmos. Sci. 75, 1029–1043. https://doi.org/10.1175/JAS-D-16-0282.1.

Klipp, C.L., Adelphi, M., 2008. A new scaling term for use in roughness sublayers. In: 18th Symp. On Boundary Layers and Turbulence, Stockholm, Sweden (9-13 June 2008). American Meteorological Society.

Kristensen, L., Jensen, N.O., 1979. Lateral coherence in isotropic turbulence and in the natural wind. Boundary-Layer Meteorol. 17, 353–373. https://doi.org/10.1007/BF00117924.

Lystad, T.M., Fenerci, A., Øiseth, O., 2018. Evaluation of mast measurements and wind tunnel terrain models to describe spatially variable wind field characteristics for long-span bridge design. J. Wind Eng. Ind. Aerod. 179, 558–573. https://doi.org/10.1016/j.jweia.2018.06.021.

Mahrt, L., 2011. Surface wind direction variability. J. Appl. Meteorol. Clim. 50, 144–152. https://doi.org/10.1175/2010JAMC2560.1.

Mann, J., 2000. Spectral velocity tensor in moderately complex terrain. J. Wind Eng. Ind. Aerod. 88, 153–169. https://doi.org/10.1016/S0167-6105(00)00046-5.

Monin, A.S., Obukhov, A.M., 1954. Basic laws of turbulent mixing in the surface layer of the atmosphere. Tr. Akad. Nauk SSSR Geophiz. Inst. 24, 163–187.

Morse, A.P., Gardiner, B.A., Marshall, B.J., 2002. Mechanisms controlling turbulence development across a forest edge. Boundary-Layer Meteorol. 103, 227–251. https://doi.org/10.1023/A:1014507727784.

NCAR, U., 2020. Weather Research and Forecasting model | MMM: Mesoscale & Microscale meteorology Laboratory. https://www.mmm.ucar.edu/weather-research-and-forecasting-model.

Norwegian Public Road Administration, 2015. N400 Handbook for Bridge Design. Directorate of Public Roads. https://www.vegvesen.no//865860/binary/1030718.

Øiseth, O., Rönnquist, A., Sigbjörnsson, R., 2013. Effects of co-spectral densities of atmospheric turbulence on the dynamic response of cable-supported bridges: a case study. J. Wind Eng. Ind. Aerod. 116, 83–93. https://doi.org/10.1016/j.jweia.2013.03.001.

Oldroyd, H.J., Pardyjak, E.R., Huwald, H., Parlange, M.B., 2016. Adapting tilt corrections and the governing flow equations for steep, fully three-dimensional, mountainous terrain. Boundary-Layer Meteorol. 159, 539–565. https://doi.org/10.1007/s10546-015-0066-0.

Panofsky, H., Larko, D., Lipschutz, R., Stone, G., Bradley, E., Bowen, A.J., Højstrup, J., 1982. Spectra of velocity components over complex terrain. Q. J. R. Meteorol. Soc. 108, 215–230. https://doi.org/10.1002/qj.49710845513.

Repetto, M., Solari, G., 2007. Wind-induced fatigue of structures under neutral and non-neutral atmospheric conditions. J. Wind Eng. Ind. Aerod. 95, 1364–1383. https://doi.org/10.1016/j.jweia.2007.02.012.

Rotach, M.W., Andretta, M., Calanca, P., Weigel, A.P., Weiss, A., 2008. Boundary layer characteristics and turbulent exchange mechanisms in highly complex terrain. Acta Geophys. 56, 194–219. https://doi.org/10.2478/s11600-007-0043-1.

Sacré, C., Delaunay, D., 1992. Structure spatiale de la turbulence au cours de vents forts sur differents sites. J. Wind Eng. Ind. Aerod. 41, 295–303. https://doi.org/10.1016/0167-6105(92)90424-9.

Samferdselsdepartementet, 2013. National Transport Plan 2014–2023 *(English Version)*. Technical Report Meld. St. 26 (2012–2013) Report to the Storting (White Paper). Norwegian Ministry of transport and communications, Oslo, Norway.

Sandvik, A.D., Harstveit, K., 2005. Study of a Down Slope Windstorm over Southern Norway, Rjukan, 16. January 2000. Norwegian Meterological Institute. Technical Report no. 18/2005.

Sathe, A., Gryning, S.-E., Peña, A., 2011. Comparison of the atmospheric stability and wind profiles at two wind farm sites over a long marine fetch in the North Sea. Wind Energy 14, 767–780. https://doi.org/10.1002/we.456.

Scanlan, R.H., 1978. The action of flexible bridges under wind, II: buffeting theory. J. Sound Vib. 60, 201–211. https://doi.org/10.1016/S0022-460X(78)80029-7.

Solari, G., Piccardo, G., 2001. Probabilistic 3-D turbulence modeling for gust buffeting of structures. Probabilist. Eng. Mech. 16, 73–86. https://doi.org/10.1016/S0266-8920(00)00010-2.

Stiperski, I., Rotach, M.W., 2016. On the measurement of turbulence over complex mountainous terrain. Boundary-Layer Meteorol. 159, 97–121. https://doi.org/10.1007/s10546-015-0103-z.

Stull, R.B., 1988. An Introduction to Boundary Layer Meteorology. Kluwer Academic Publishers, Dordrecht, Netherland. https://doi.org/10.1007/978-94-009-3027-8.

Tamura, Y., Iwatani, Y., Hibi, K., Suda, K., Nakamura, O., Maruyama, T., Ishibashi, R., 2007. Profiles of mean wind speeds and vertical turbulence intensities measured at seashore and two inland sites using Doppler sodars. J. Wind Eng. Ind. Aerod. 95, 411–427. https://doi.org/10.1016/j.jweia.2006.08.005.

Touma, J.S., 1977. Dependence of the wind profile power law on stability for various locations. J. Air Pollut. Contr. Assoc. 27, 863–866. https://doi.org/10.1080/00022470.1977.10470503.

Vickers, D., Mahrt, L., 1997. Quality control and flux sampling problems for tower and aircraft data. J. Atmos. Ocean. Technol. 14, 512–526. https://doi.org/10.1175/1520-0426(1997)014¡0512:QCAFSP¿2.0.CO;2.

Weber, R.O., 1999. Remarks on the definition and estimation of friction velocity. Boundary-Layer Meteorol. 93, 197–209. https://doi.org/10.1023/A:1002043826623.

Wieringa, J., 1992. Updating the Davenport roughness classification. J. Wind Eng. Ind. Aerod. 41, 357–368. https://doi.org/10.1016/0167-6105(92)90434-C.

Wilczak, J.M., Oncley, S.P., Stage, S.A., 2001. Sonic anemometer tilt correction algorithms. Boundary-Layer Meteorol. 99, 127–150. https://doi.org/10.1023/A:1018966204465.

Wyngaard, J.C., 1973. On the surface-layer turbulence. In: Workshop on Micrometeorology. American Meteorological society, Boston, USA, pp. 101–149.

Yuan, J., Jouybari, M.A., 2018. Topographical effects of roughness on turbulence statistics in roughness sublayer. Phys. Rev. Fluid. 3, 114603. https://doi.org/10.1103/PhysRevFluids.3.114603.

Zeman, O., Jensen, N.O., 1987. Modification of turbulence characteristics in flow over hills. Q. J. R. Meteorol. Soc. 113, 55–80. https://doi.org/10.1002/qj.49711347505.